2010-01

Sensitivity experiments for ensemble forecasts of the extratropical transition of typhoon Tokage (2004)

Anwender, Doris

Anwender D, Jones SC, Leutbecher M, Harr PA. 2010. Sensitivity experiments for ensemble forecasts of the extratropical transition of typhoon Tokage (2004). Quarterly Journal of þÿthe Royal Meteorological Society, 136: 183 200. DOI:10.1002/qj.527

RMetS
Royal Meteorological Society

Sensitivity experiments for ensemble forecasts of the extratropical transition of typhoon *Tokage* (2004)

Doris Anwender,[a]* Sarah C. Jones,[a] Martin Leutbecher[b] and Patrick A. Harr[c]
[a]*Institut für Meteorologie und Klimaforschung, Karlsruhe Institut of Technology, Karlsruhe, Germany*
[b] *European Centre for Medium Range Weather Forecasts, Reading, UK*
[c] *Department of Meteorology, Naval Postgraduate School, Monterey, California*
*Correspondence to: Doris Anwender, Institut für Meteorologie und Klimaforschung, Universität Karlsruhe, 76131 Karlsruhe, Germany. E-mail: doris.anwender@imk.uka.de

The extratropical transition (ET) of tropical cyclones often has a detrimental impact on predictability in the vicinity of the event and downstream. Ensemble forecasts provide an appropriate means by which to investigate both the uncertainty and the dynamical development leading to the different ET scenarios. Sensitivity experiments are presented using the European Centre for Medium-Range Weather Forecasts (ECMWF) ensemble prediction system (EPS) to investigate different methods of perturbing the ensemble forecast of the ET of Typhoon *Tokage* (2004). During ET these perturbations have a notable impact on the ensemble spread representing the uncertainty. Three experiments were performed: one of them without singular vectors (SVs) targeted on the tropical cyclone, the second without stochastic physics and the third excluding both perturbation methods.

The targeted perturbations are most important for sufficient spread in track and intensity. Without the targeted perturbations, the analysis is not contained within the ensemble spread. Stochastic physics leads to stronger reintensification of the ensemble members after ET. The higher track spread leads to higher variability in processes such as lower tropospheric latent heat release. This can be related to a higher spread in the upper-level midlatitude flow for both perturbation methods. A connection is drawn between the strength of ET and the modification of the downstream midlatitude flow pattern. The uncertainty due to the targeted perturbations propagates downstream with a Rossby wave train excited during *Tokage*'s ET. For the case of stochastic physics, the uncertainty spreads to the ridge directly downstream of the ET system but is not evident further downstream.

Key Words: ensemble prediction; tropical cyclone

Received 14 April 2009; Revised 31 July 2009; Accepted 16 September 2009; Published online in Wiley InterScience 15 January 2010

Citation: Anwender D, Jones SC, Leutbecher M, Harr PA. 2010. Sensitivity experiments for ensemble forecasts of the extratropical transition of typhoon *Tokage* (2004). *Q. J. R. Meteorol. Soc.* **136**: 183–200. DOI:10.1002/qj.527

1. Introduction

A tropical cyclone (TC) transforming into an extratropical system often causes a decrease in predictability (Harr *et al.*, 2008). The complex physical processes involved in the structural changes during an extratropical transition (ET) event contribute to difficulties in the forecast of such events. Furthermore, uncertainties can arise through small position errors of the decaying TC relative to an approaching midlatitude trough (Klein *et al.*, 2002; Ritchie and Elsberry, 2007). These errors can grow strongly, since small phasing errors can have a large impact on the forecast track and intensity as the TC enters the midlatitude flow (Jones

et al., 2003). Additionally, small errors can grow in the downstream flow (McTaggart-Cowan *et al.*, 2003, 2004).

Ensemble prediction has been established as a method to quantify the predictability of a given atmospheric scenario (Lewis, 2005). An ensemble prediction system (EPS) is initialized by adding small-amplitude perturbations, so-called initial perturbations, to the analysis. The amplitude of the initial perturbations should be commensurate with the estimates of the magnitude of typical analysis errors arising, for example, through insufficient or regionally and temporally heterogeneous data coverage over the globe. The dispersion with time of the initially very similar atmospheric scenarios gives a measure of the uncertainty in the forecast and the extent of possible error growth.

In the European Centre for Medium-Range Weather Forecasts (ECMWF) EPS 51 forecasts with lower resolution are calculated in addition to the high-resolution deterministic forecast. The initial perturbations are constructed at ECMWF using singular vectors (SVs), which describe the fastest error growth over a finite time interval (Farrell, 1982; Leutbecher and Palmer, 2008).

At ECMWF, SV growth is optimized for the extratropical domain (i.e. polewards of 30°) and for the tropical domain separately. As targeting SVs on the whole tropical strip would not guarantee that fast-growing SVs will also be in the region of a TC, SVs are targeted on optimization regions around the forecast location of TCs (Barkmeijer *et al.*, 2001; Puri *et al.*, 2001).

If one had a perfect model, all uncertainties would be described by the initial perturbations. However, in every model run additional uncertainties arise due to small-scale physical processes that are not resolved and therefore have to be parametrized. Model errors are also associated with properties of the large-scale flow (e.g. large-scale condensation) and with uncertainties in the numerics. The ECMWF ensemble takes these into account by perturbing the ensemble additionally through multiplying the parametrized tendencies of every ensemble member with random numbers at every grid point (Buizza *et al.*, 1999). This approach is known as stochastic physics. Temporal and spatial coherence of the tendency perturbations is enforced by using the same random number over six model time steps and within a tile of 10° by 10° in latitude and longitude.

An EPS forecast of an ET case contains a range of scenarios (Anwender *et al.*, 2008; Harr *et al.*, 2008). In this article we try to gain information about the origin of the different dynamic developments of the ET scenario by carrying out experiments with the ECMWF EPS. By applying the perturbation methods to the EPS in a certain manner, we expect to alter the ET representation. We suppose that both the moist SVs targeted on the TC and the stochastic physics are important for ET. The dispersion and downstream propagation of their impact yields a measure of how far the reduction of predictability due to an ET can extend.

An overview of the case investigated and the experimental set-up is given in section 2. The impact of initial perturbations and stochastic physics on track and intensity spread of the TC ensemble forecast is presented in section 3. The dynamics of the downstream propagation of the perturbations in the EPS are explored in section 4. The spread and diversity of the synoptic patterns shown by the individual ensemble members in the experiments are investigated by grouping them into clusters using the method of Harr *et al.* (2008). The behaviour of the ensemble members in runs with stochastic physics perturbations is compared with that in runs with targeted perturbations. In section 5 conclusions, together with outstanding questions and future directions, are given.

2. Experimental set-up

Typhoon *Tokage* (2004) was chosen for the experiments because it seemed to have a strong influence on the building of a trough–ridge–trough pattern, consisting of the trough that interacted with the TC, a ridge directly downstream and a second trough downstream of the ridge (Anwender *et al.*, 2008). Before ET, the midlatitude flow upstream of *Tokage* was zonally oriented.

When the TC approached the strong potential temperature gradient on the dynamic tropopause (defined here as the 2 PVU potential vorticity (PV) surface, with 1 PVU = 10^{-6} K m^2 kg^{-1} s^{-1}) and the outflow of *Tokage* interacted with the midlatitude jet, a ridge downstream of *Tokage* amplified dramatically (Figure 1). *Tokage* completed ET at 0000 UTC on 21 October and reintensified thereafter (JMA, 2004). During the ET of *Tokage*, the dispersion of the EPS was enhanced around the ET for two days from the time of ET and downstream of the ET from three days after the ET (Anwender *et al.*, 2008).

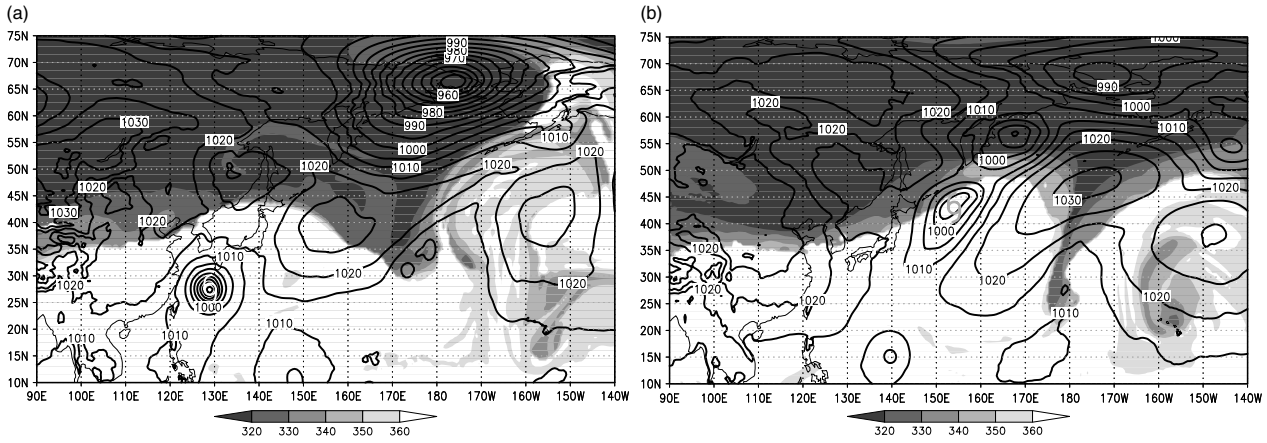

Figure 1. Analysis of *Tokage* at (a) 1200 UTC on 19 October 2004 (*Tokage*'s position at about 130°E, 28°N) and (b) 1200 UTC on 21 October 2004 (*Tokage*'s position at about 153°E, 43°N). *Tokage* is marked by a TC symbol. Shown are potential temperature on the dynamic tropopause (shaded, K) and surface pressure (contours, hPa) (taken from Anwender *et al.*, 2008).

The variability associated with the ET of *Tokage* was highest for the operational ensemble forecast from 1200 UTC on 16 October 2004. Therefore, this date has been chosen as the initialization time for the sensitivity experiments. The optimization region for *Tokage* at this date will be shown in section 4.

In the experiments, new ten-day ensemble forecasts of *Tokage* were calculated with the ECMWF EPS. Cycle 29R2 was used for the calculations, which differs from the cycle used operationally at the time of *Tokage*'s life-cycle. The SVs were recalculated in order to be consistent with the model cycle used for the experiments. At the ECMWF the optimization region around a TC is determined such that a rectangular box is placed around the TC positions forecast for the optimization time, i.e. 48 h, by the most recent ensemble forecast. During an ET this optimization region will start to overlap with the optimization region for the extratropical SVs (polewards of 30° latitude). To avoid the duplication of structures in the set of extratropical SVs, the SVs targeted on a TC are computed in the subspace orthogonal to the set of extratropical SVs (Leutbecher, 2007). A minimum extension of this box of 10° in latitude and 14° in longitude is imposed. The EPS was calculated with $T255L40$ resolution and the SVs with $T42L40$.

Four experiments were performed. In the first one both the initial perturbations targeted on *Tokage* and the stochastic physics were switched off. This experiment will be referred to as 'Nopert/Nosto'. The second experiment ('Pert/Nosto') was calculated with the targeted initial perturbations but without stochastic physics. In the third experiment ('Nopert/Sto') only the perturbations on *Tokage* were switched off. The stochastic physics remained switched on. The fourth experiment ('Pert/Sto') included both targeted perturbations and stochastic physics. As our focus lies on the investigation of the representation of the dynamics of ET in the EPS experiments, and because of the high computational costs, we ran experiments for one ET case and initialization time.

The difference between Pert/Nosto and Nopert/Nosto yields a measure of the influence of the perturbations targeted on *Tokage* on the description of uncertainties in the ensemble. By switching off the stochastic physics, this influence is confined solely to that associated with the targeted perturbations.

The difference between Nopert/Sto and Nopert/Nosto is investigated to obtain information about the influence that uncertainties in the physical processes alone have on the ensemble forecasts during the ET of *Tokage*. Pert/Sto was investigated to get information about whether the combined influence of the targeted perturbations and the stochastic physics differs from their individual influences. Pert/Sto has the same configuration as the operational ensemble forecast, but the cycle (29R2) is different.

The analysis method of Harr *et al.* (2008) is applied to group members of similar synoptic developments into distinct clusters. The method allows for the investigation of the large number of 51 ensemble members in a compact way. The method consists of an empirical orthogonal function (EOF) analysis, combined with a fuzzy clustering of the first two principal components. We applied the method to the potential temperature on the dynamic tropopause of the 51 ECMWF ensemble members. By the aid of this method, the regions of highest variability in the ensemble can be identified and the ensemble members contributing in a similar manner to these regions can be grouped together. Harr *et al.* (2008) and Anwender *et al.* (2008) found that the variability in the large-scale features associated with six cases of ET could be characterized by the first two EOFs. This is confirmed by the variability patterns of the ensemble members (not shown) in the experiments presented here.

Four clusters are obtained in both Pert/Nosto and Pert/Sto and three in both Nopert/Nosto and Nopert/Sto for the clustering time of 0000 UTC on 21 October, i.e. the ET time. An overview of all the clusters for all the experiments is given in Table I.

3. Influence on ET of *Tokage*

The aim of ensemble forecasting is to predict the probability of an event that matches the percentage of occurrences of this event. This property is called the reliability of an ensemble forecast. If a forecast event occurs for the same percentage of cases with which it is forecast, the reliability is optimal. Furthermore, an ensemble forecast should have a high resolution, i.e. the probability density function should be sharp. A high resolution implies that the forecast probability of the occurrence of an event is distinctly different from the climatological probability of that event occurring, while a forecast with a probability close to the climatological probability of the event occurring represents a very low resolution.

A good reliability implies that the spread of the ensemble members contains the analysis most of the time and that some members lie close to the analysis (Puri *et al.*, 2001). If the analysis lies outside the ensemble spread too frequently, the spread is too small.

In this section we show tracks and intensity forecasts for three of our four EPS experiments. In the interest of brevity the results for Pert/Sto are only mentioned briefly. We consider the individual reliability of *Tokage*'s track forecast, although we do not attempt to investigate the reliability of the ensemble in a statistical sense. Our focus lies on the sensitivity of the track and intensity forecast to ET in the ensemble.

3.1. *Tracks*

The ensemble track forecasts for *Tokage* based on the central mean-sea-level pressure are compared for Pert/Nosto (Figure 2(a)), Nopert/Nosto (Figure 2(b)) and Nopert/Sto (Figure 2(c)), along with the analysis, the deterministic forecast and the JMA (2004) best track.

A distinct difference between Pert/Nosto and Nopert/Nosto can be seen around the recurvature time (60 h after initialization). In Pert/Nosto (Figure 2(a)) the locations of the outermost ensemble members are separated by more than 500 km. Both the analysis, in good agreement with the best track at this time, and the deterministic forecast lie close to the edge of, but fall within, the ensemble tracks. In the case of Nopert/Nosto (Figure 2(b)) the deterministic forecast lies at the edge of the ensemble tracks and the analysis even outside for 48 h and 60 h forecast lead times. The spatial separation of the ensemble members is only about 200 km. The track forecast in the Nopert/Sto runs (Figure 2(c)) shows slightly higher spread around the recurvature than Nopert/Nosto, such that the analysed track

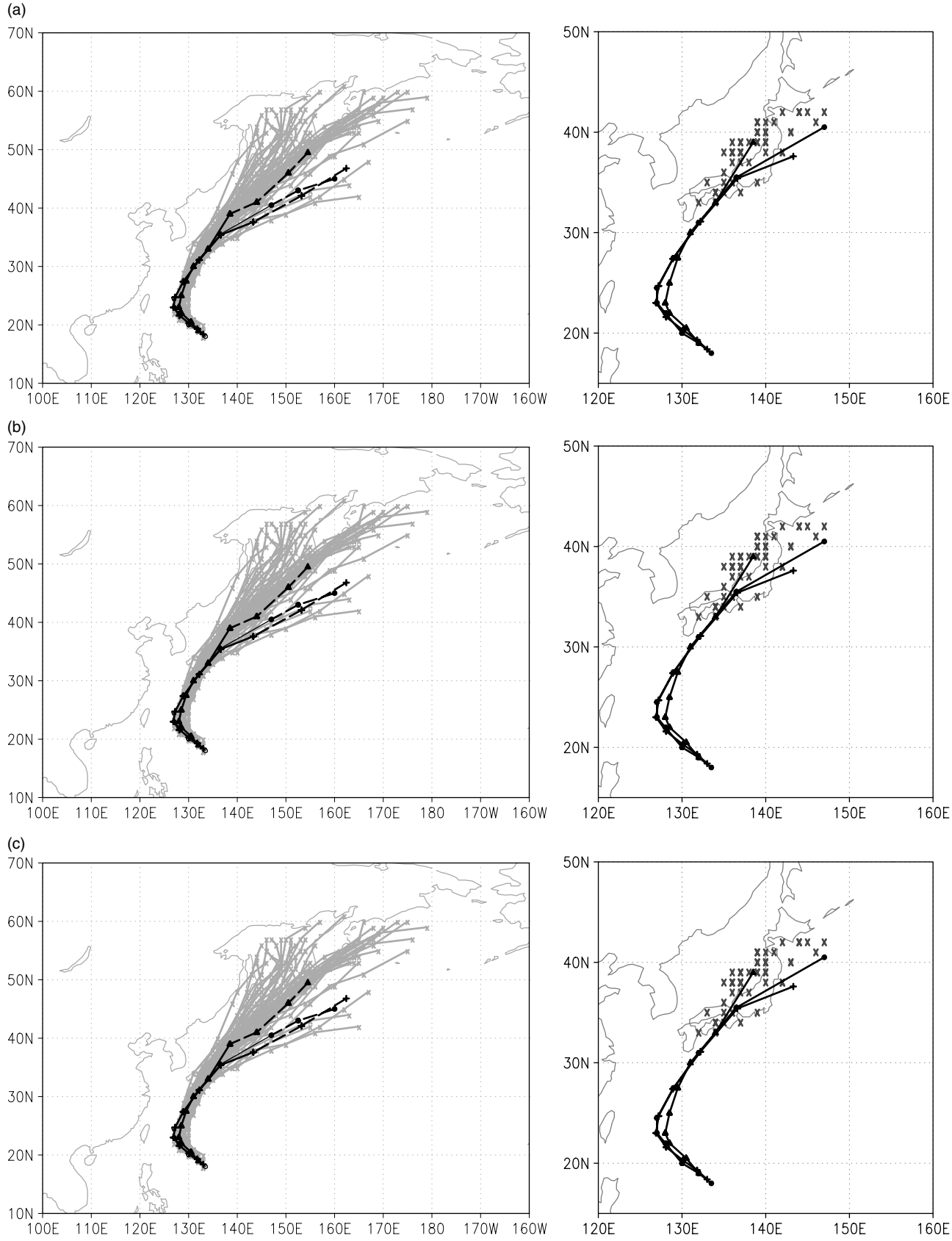

Figure 2. Tracks for *Tokage* based on the location of minimum sea-level pressure for (a) Pert/Nosto, (b) Nopert/Nosto and (c) Nopert/Sto runs. Shown are the ECMWF analysis (black line with circles), best track (black line with crosses), deterministic forecast (black line with triangles) and ensemble forecast (grey) initialized at 1200 UTC on 16 October for 7 days. The analysis is dashed after ET. Right lower corner: positions of the ensemble members at 0000 UTC on 20 October, i.e. ET time (dark grey × symbols), analysis, best track and deterministic forecast shown until 0000 UTC on 20 October (i.e. ET time) only.

Table I. Overview of all clusters for all experiments with the ECMWF EPS: number of clusters found, number of members in each of the clusters, percentage contribution of EOF 1 and EOF 2 to the total variability. Contribution of the individual clusters (+ positive, - negative, o no contribution) to the respective variability pattern (EOF). Strength of ET: 0: no ET; 1: little or no reintensification, central mean-sea-level pressure $\geq$ 1000 hPa; 2: moderate reintensification, central mean-sea-level pressure 985–999 hPa; 3: deep reintensification, central mean-sea-level pressure $<$ 985 hPa (similar to Klein *et al.* (2000)).

	Clusters	Members	EOF 1	Contrib.	EOF 2	Contrib.	ET	Fig.
				Resolution *T*255*L*40				
Pert/ Nosto	4	11	18.4 %	+	11.2 %	-	0	9a, 10a, 11a
		12		-		-	3	/
		8		+		+	3	/
		14		o		+	3	9b, 10b, 11b
Nopert/ Nosto	3	14	20.7 %	+	10.1 %	o	3	9d, 10d, 11d
		18		-		+	3	/
		11		-		-	2	9c, 10c, 11c
Pert/ Sto	4	9	19.2 %	+	9.9 %	-	2	/
		13		-		-	3	/
		10		+		+	3	/
		11		-		+	3	/
Nopert/ Sto	3	19	19.3 %	o	9.6 %	+	3	/
		14		-		-	3	/
		9		+		-	3	/

is at the edge of the ensemble tracks or slightly outside only at 60 h forecast lead time.

Close to ET time in Nopert/Nosto and Nopert/Sto (Figure 2(b) and (c)), the analysis and the best track are in the vicinity of the three (Nopert/Nosto) to five (Nopert/Sto) southernmost ensemble members and separated from the main group that follows the deterministic forecast. After ET they lie in the gap between the southerly and main groups of ensemble members, such that no member overlaps with the analysis or with the best track. In Pert/Nosto (Figure 2(a)), several members overlap with the analysis and best track around ET time and a few more members than in Nopert/Nosto can be found south of the analysis and best track. No clear gap can be seen in Pert/Nosto. Consequently, Pert/Nosto is a more skillful probabilistic forecast than the two forecasts without the perturbations targeted on *Tokage*.

The tracks for Pert/Sto (not shown) are very similar to those for Pert/Nosto (Figure 2(a)), but one member in addition shows a track south of the analysis and the best track after ET. Hence, the spread for Pert/Sto is slightly higher than for Pert/Nosto.

The forecast positions of the decaying TC are shown at the analysed ET time (bottom right corner of Figure 2(a)–(c)). Comparing the analysis and the best track, which are only shown until the ET time, illustrates that in the analysis the ET system moves too quickly. In Pert/Nosto the possible ET positions are more widely spread than in both Nopert/Nosto and Nopert/Sto. There are more members showing the storm around southern Japan at the analysed ET time, i.e. a slow movement of the storm. In Pert/Nosto and Nopert/Sto (Figures 2(a) and (c)), more TC positions than in Nopert/Nosto (Figure 2(b)) are distributed around the analysis. Pert/Nosto shows the most TC positions around the best track. Most of the forecast positions of *Tokage* in Nopert/Nosto are confined to a region north of the analysis and the best track. Hence, quite a high probability is assigned to erroneous position forecasts. Even though in Pert/Nosto a number of the forecast TC positions, especially those showing the slow TC motion, are far from the best track, the broad distribution of probable positions indicates the uncertainty in the forecast more appropriately.

The distribution of TC positions at ET time in Pert/Sto (not shown) looks similar to that in Pert/Nosto. Three members in addition show slow movement and are located close to southern Japan at ET time. Two members in addition to Pert/Nosto show positions close to the best track. The spread of ET positions is largest in Pert/Sto.

It is seen that the SVs targeted on *Tokage* produce the most members close to the analysis and the best track. Through their generally rather large scales, they perturb the broad structures and the environment around the TC, and are resolved sufficiently by the global model to have some skill in forecasting TC tracks (Puri *et al.*, 2001). Except for the run with both targeted perturbations and stochastic physics, Pert/Nosto is the most skillful track probability forecast. The runs with only stochastic physics yield a slightly better agreement with the analysis and the best track at recurvature than the Nopert/Nosto runs, but, as many members show a track too far to the north, a high probability is assigned to a track far from the analysis. The uncertainty around both the recurvature and the ET is still under-represented. Consequently, the stochastic physics alone cannot account for the uncertainties associated with the ET of *Tokage*. The stochastic physics is mainly responsible for enhancing the downstream spread at later forecast times (section 4).

3.2. *Central mean-sea-level pressure*

The four experiments are further examined with regard to their representation of TC intensity in terms of the central mean-sea-level pressure (Figure 3). The resolution of the operational model that has been used to calculate the deterministic forecast is twice as high as that of the ensemble. Therefore the deterministic forecast is expected to show a much deeper central pressure for *Tokage* than the ensemble in the stage when it is still a tropical cyclone. Moreover, it is not surprising that the best track central pressure lies far from the analysis, since global models like the ECMWF Integrated Forecasting System (IFS) do not have adequate resolution to represent the inner cores of TCs accurately. However, both analysis and best track show a steep increase of central pressure from 0000 UTC–1200 UTC on 20 October (Figure 3, 84–96 hours after initialization of the forecast). Between these two times, *Tokage* made landfall and weakened considerably. From 1200 UTC on 20 October, the central pressure of the analysis and best track are in close agreement.

Shortly after initialization time the spread of central pressure in Nopert/Nosto (Figure 3(b)) is much smaller than in Pert/Nosto and Nopert/Sto (Figure 3(a) and (c)). In the latter, a notable spread can already be seen at short forecast times. All three experiments shown contain different representations of the weakening of the intensity in the ensemble members around 84–108 h and of the reintensification of all but one member in Pert/Nosto and two members in Nopert/Sto around 120–144 h forecast lead time. At the 96 and 108 h forecast, the analysis and the best track have pressure values higher than the ensemble members in all the experiments including Pert/Sto (not shown). In Pert/Nosto some members show a weakening of intensity about 12–24 h later than the analysis, but only two of them reach the high pressure values seen in the analysis and in the best track. In Nopert/Sto (Figure 3(c)), a comparable weakening is also seen for two members, but the rest of the members stay below 980 hPa central mean-sea-level pressure until 156 h forecast lead time. The deep pressures in Nopert/Sto (Figure 3(c)) reintensify even more strongly than in Nopert/Nosto (Figure 3(b)). At 144 h forecast lead time, the central pressures of all but the three weak members in Nopert/Sto are below 965 hPa.

In Pert/Nosto, several members have quite high central pressure values, ranging from 980–990 hPa between 108 and 120 h. These higher values are seen in Pert/Sto (not shown) also, but *Tokage* does not weaken to pressure values higher than 990 hPa before reintensification in any member of Pert/Sto. The spread in Pert/Sto is slightly higher towards the end of the forecast interval, and one member with a pressure value below 930 hPa is seen for the 132 h forecast interval.

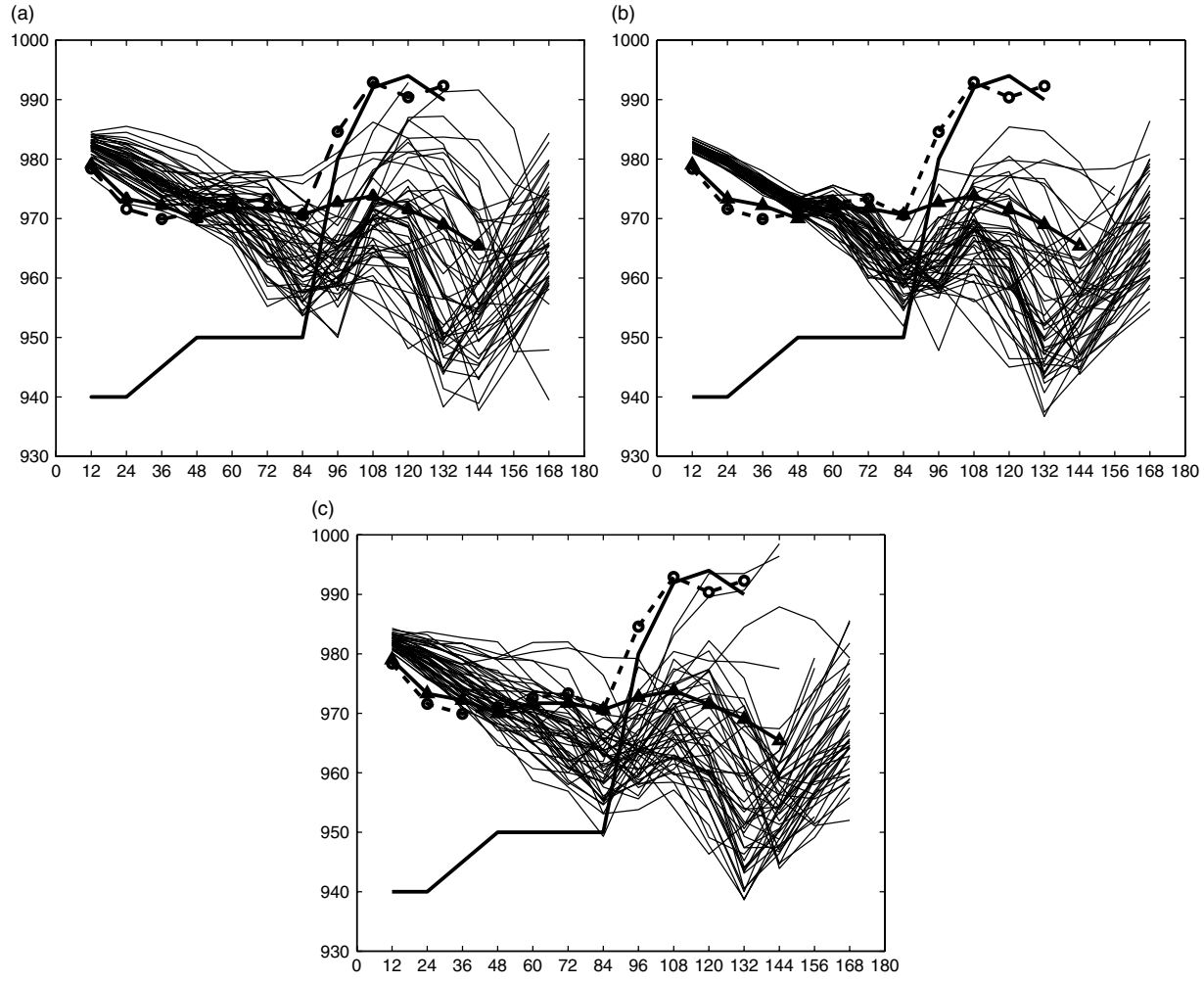

Figure 3. Analysis (thick black line with circles), best track (thick black line), deterministic forecast (thick black line with triangles) and ensemble forecast (thin black lines) of the central mean-sea-level pressure of *Tokage* initialized at 1200 UTC on 16 October 2004 for (a) Pert/Nosto, (b) Nopert/Nosto and (c) Nopert/Sto.

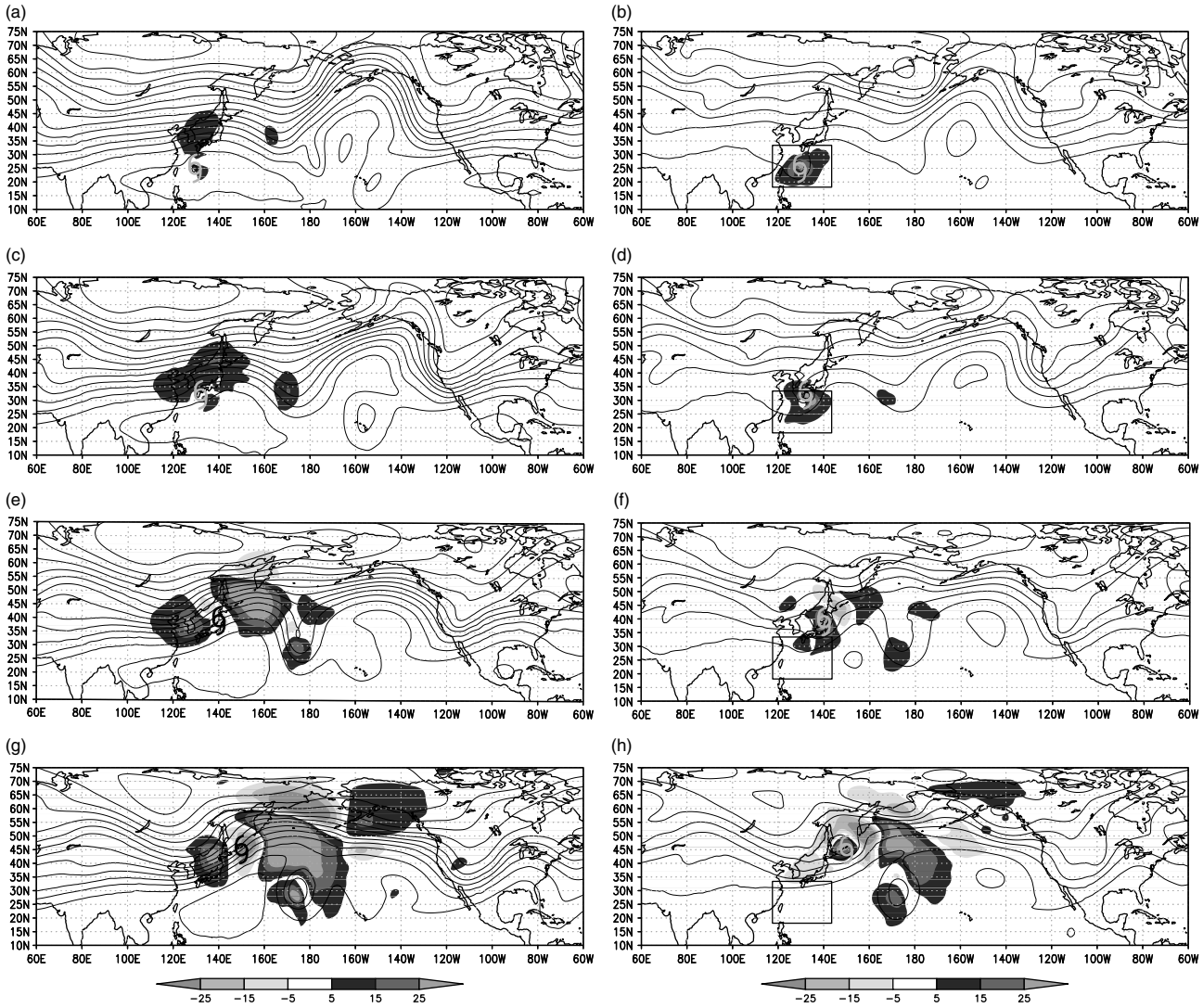

Figure 4. RMSD difference of the geopotential height (m) at 200 hPa (left) and 500 hPa (right) between the ensemble forecasts initialized at 1200 UTC on 16 October with and without targeted perturbations on *Tokage* (shaded). Forecasts are for (a,b) 0000 UTC on 19 October, i.e. 48 h prior to ET, (c,d) 0000 UTC on 20 October, i.e. 24 h prior to ET, (e,f) 0000 UTC on 21 October, i.e. ET time and (g,h) 0000 UTC on 22 October, i.e. 24 h after ET. The ECMWF control forecast of geopotential height is shown by thin black contours. The position of *Tokage* in the control forecast is marked by a hurricane symbol. The optimization region in which the targeted SVs optimize at 1200 UTC on 18 October is marked by a black box.

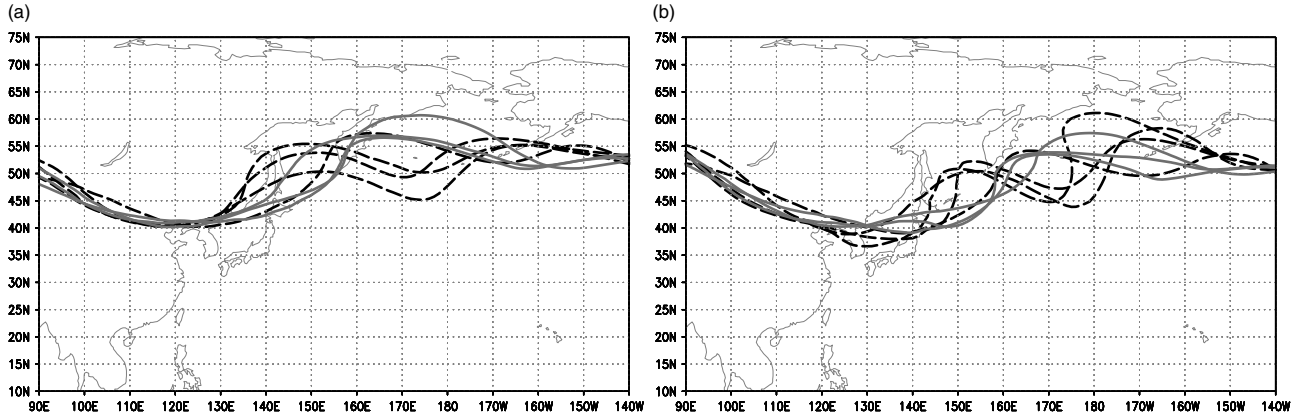

Figure 5. Spaghetti plots of (a) the 1150 gdam geopotential height at 200 hPa and (b) the 545 gdam geopotential height at 500 hPa of the most outlying ensemble members initialized at 1200 UTC on 16 October for Pert/Nosto (black, dashed) and Nopert/Nosto (grey), verified at 0000 UTC on 22 October, i.e. 24 h after ET (corresponding to the time of Figure 4(g) and (h)).

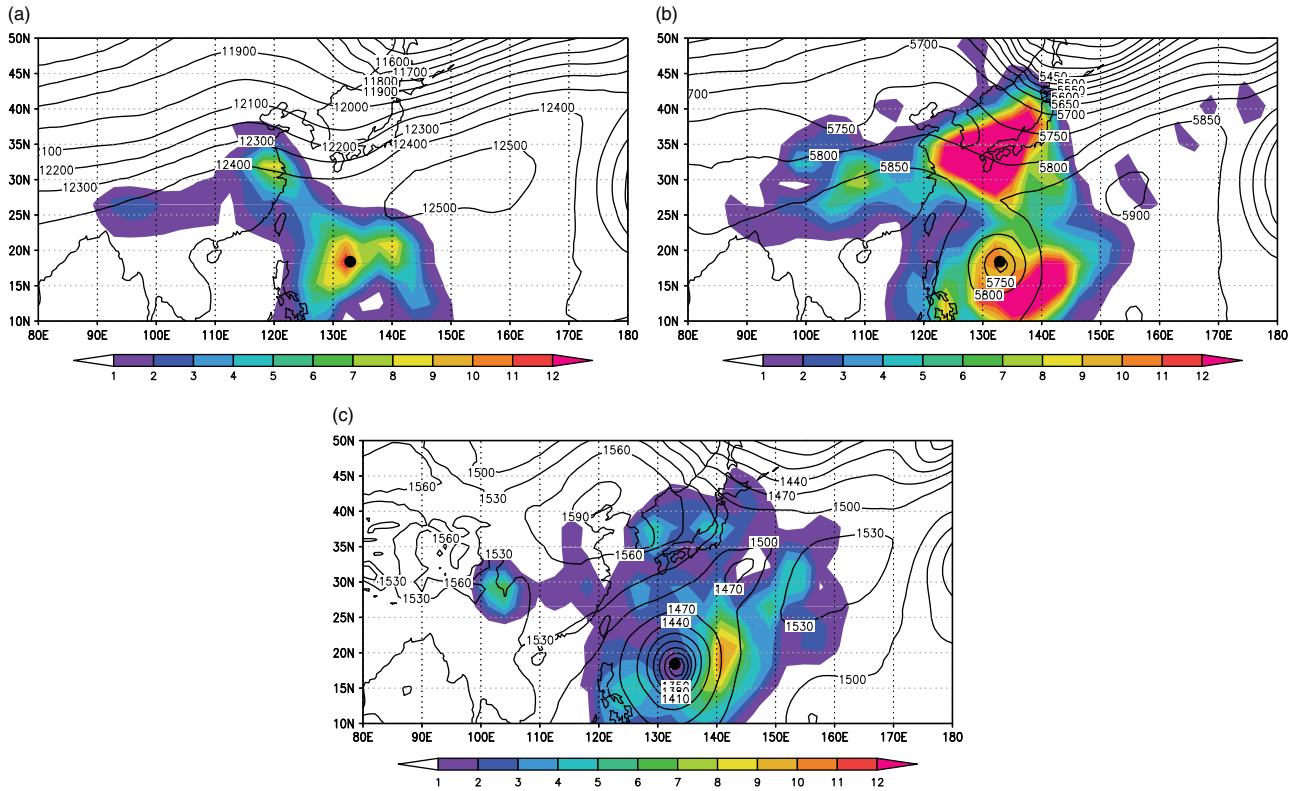

Figure 6. Total dry energy (J kg^{-1} × 1000, shaded) of the leading five initial SVs targeted on *Tokage*, weighted with their singular value, at (a) model level 10 (about 200 hPa), (b) model level 20 (about 500 hPa) and (c) model level 29 (about 850 hPa) for 1200 UTC on 16 October 2004. Geopotential height of the control forecast for 1200 UTC on 16 October at the respective level is also shown (m, grey). *Tokage* is marked by a black dot.

Puri *et al.* (2001) showed that the use of SVs in the Tropics leads to a slightly higher spread, but mainly to an overall weakening of the TC in the ensemble forecast compared with their control ensemble forecast for two Pacific cases. In contrast, our results for *Tokage* indicate that the use of SVs targeted on the TC leads instead to a much larger spread of the pressure values. Hence, more possible ET scenarios are produced due to the SVs, ranging from ET with strong reintensification to no-ET scenarios. The wider variety of pressure values after the reintensification is due to the wider distribution of TC positions (Figure 2) relative to the midlatitude potential temperature gradient with which the TCs interact.

Two Pert/Nosto and two Nopert/Sto members show a weakening in intensity to pressure values above 990 hPa. For one of these members (both in Pert/Nosto and Nopert/Sto), the reason for the weakening does not lie in the landfall, as the track lies south of Japan. The midlatitude trough passes rapidly to the north of the decaying TC without interaction. The other member weakens due to landfall, corresponding to the analysis of *Tokage*, but with a delay of about 24 h in the Pert/Nosto (Figure 3(a)) and 12 h in the Nopert/Sto (Figure 3(c)) case. In these members the ex-TC reintensifies strongly, however, unlike in the analysis.

The strong growth of spread in the central pressures together with the weak growth in track spread of Nopert/Sto (Figure 2(c)) at forecast times before the ET time is similar to the results of Puri *et al.* (2001). They found that the stochastic physics leads to a smaller spread in the TC tracks than targeted initial perturbations, but a much larger spread in the central pressures. They attribute large variations in the central pressures to convective forcing in the stochastic physics.

In contrast to the results of Puri *et al.* (2001), however, the intensity spread in Nopert/Sto before the ET time was only slightly larger than in Pert/Nosto, and after the ET time the spread in central pressures due to the targeted SVs (Figure 3(a)) was much larger than that due to the stochastic physics (Figure 3(c)). On average, the stochastic physics yields deeper pressure values than the targeted SVs, but the variety is smaller. Although two members weaken considerably, there are no members showing moderate weakening after ET and moderate deepening thereafter.

During the ET of *Tokage*, the uncertainty in the intensity forecast is generated by uncertainties in flow features with larger scales rather than processes contributing to the stochastic physics. Uncertainty is associated with variations in the TC position, variations in the strength of the potential temperature gradient in the midlatitudes and uncertainties in the phasing of the TC and the midlatitude trough. The rather large spread of TC locations in Pert/Nosto around the recurvature time leads to more different positions of the TCs relative to the baroclinic zone during ET. This results in differing strengths of interaction, and therefore in a wider range of intensities after ET in Pert/Nosto than in Nopert/Nosto and Nopert/Sto. To a lesser extent this can be found also in Nopert/Sto compared with Nopert/Nosto. The perturbation of physical processes generates only a small part of the intensity variations during *Tokage*'s ET. For Pert/Sto the spread is equally large, but the ensemble mean is deeper.

4. Downstream impact

In this section we investigate how the dynamics of an ET enhance the ensemble spread, consider which of the perturbation methods plays the major role, and discuss

the mechanisms by which the enhanced spread propagates downstream. We quantify the uncertainty that is introduced into the ensemble forecast through the ET of *Tokage* by determining the difference of spread in these pairs of experiments. The effect of each of the perturbation methods is considered individually and then the experiment with the combination of both targeted perturbations and stochastic physics, Pert/Sto, is described briefly.

The root-mean-square difference (RMSD) has been chosen as a measure of spread. The RMSD determines the average distance of all the ensemble members to the control forecast. The differences between the RMSDs are referred to as the signal of the respective method of perturbation. Taking the RMSD as a measure of spread has the advantage that the same reference, i.e. the control forecast, is used in all four experiments. In contrast the standard deviation, another measure of spread, has the ensemble means as reference. So there would be a difference in the references of the experiments.

4.1. Signal of the perturbations targeted on *Tokage*

4.1.1. Origin and downstream propagation

Two days before *Tokage* underwent ET, the typhoon can be seen at about 130°E and 25°N (Figure 4(a) and (b)). At this forecast time a small-scale positive part of the signal is located around *Tokage* and a larger-scale one north of it in the midlatitudes at 200 hPa (Figure 4(a)), indicating enhanced spread due to the targeted perturbations. At 500 hPa (Figure 4(b)) a signal of high positive values can be found around *Tokage*. At this time the higher spread in Pert is mainly generated by the wider variety of TC locations shown by the ensemble (Figure 2(a) and (b)). Additionally, the intensity difference at 60–84 h forecast time is slightly higher in Pert than in Nopert (Figure 3(a) and (b)). The signal is confined to the area around the TC shortly before ET at 500 hPa (Figure 4(b) and (d)), while at 200 hPa (Figure 4(a) and (c)) the large-scale part of the signal can be found in the midlatitudes north of the TC. A small-scale part of the signal is seen downstream of the TC as well. The signal at 500 hPa does not seem to grow either in amplitude or in scale until the ET time. In contrast, strong growth of the signal at 200 hPa in the midlatitudes can be seen in regions of high baroclinicity, defined by a strong gradient in geopotential.

At the ET time (Figure 4(e) and (f)), the signal in the midlatitudes grows strongly. As seen in the TC track forecasts at the ET time (Figure 2(a), small box), the TC positions vary notably, which contributes significantly to the signal around *Tokage* at 500 hPa. One part of the signal at 200 hPa is associated with an approaching upstream trough. The part of the signal with the largest scale is due to variability of the ridge directly downstream of *Tokage*. Other parts of the signal grow in the cut-off low downstream of that ridge at about 175°E.

The perturbations targeted on *Tokage* lead to a phase shift of the regions of high variability in the ensemble members between Pert/Nosto and Nopert/Nosto. This is seen in the regions of the negative parts of the signal (Figure 4(e)–(h)). To illustrate, this some of the most extreme members of the Pert/Nosto and Nopert/Nosto runs are compared (Figure 5). The members contributing most strongly to the variability in the ensemble, i.e. those that had the highest PCs, have been selected from each of the clusters for Pert/Nosto and Nopert/Nosto (Table I). Negative parts of the signal (Figure 4(g)) were seen at locations at which the variability in Nopert/Nosto is higher than that in Pert/Nosto, e.g. at about 150°E at 200 hPa (Figure 5(a)). Another distinct shift at 200 hPa is seen at about 180°E, where higher spread in Pert/Nosto (black, dashed) is seen south of 55°N and higher spread in Nopert/Nosto (grey) north of 55°N. The northernmost member of Pert/Nosto and the southernmost member of Nopert/Nosto overlap in this region (Figure 5(a)). A shift of the regions of largest spread between the Pert/Nosto and Nopert/Nosto members at 500 hPa is obvious in the region from about 150°E–180°E (Figure 5(b)). This leads to the couplet of negative values at 65°N and positive values centred on 45°N seen at 160°E in the RMSD signal (Figure 4(g) and (h)) of the targeted perturbations.

To illustrate the origin of the disturbances, the horizontal and vertical structure of the leading five initial SVs (SV1–5) weighted with their singular values are investigated using the total energy (Figure 6). The total energy norm is used at the ECMWF to determine the growth of SVs. At 200 hPa (Figure 6(a)), rather small-amplitude structures can be found in the trough and the ridge upstream, while the largest structures are seen directly around *Tokage*. The largest amplitude of SV1–5 at 500 hPa can be found in the midlatitudes directly north of *Tokage*, between a ridge and a trough in the geopotential, but also southeast and at the centre of the TC (Figure 6(b)). At 850 hPa (Figure 6(c)), the highest amplitudes are located east of the typhoon and in the western part of the ridge located at about 150–170°E and 25–35°N. Perturbations to this ridge would be expected to influence *Tokage*'s track. We conclude that the initial perturbation growth that leads to the enhanced spread seen in Figure 4(a) and (c) affects both the trough–ridge–trough structure in the midlatitudes and the TC.

The farthest location to which the signal can propagate is the leading edge of a packet of waves that is also the most likely location of downstream cyclogenesis (Szunyogh *et al.*, 2002). The ridge building from 0000 UTC on 20 October attributed to the outflow of *Tokage* can be seen as a dipole in the meridional wind component at 125–170°E (Figure 7). The couplets of positive and negative values of the meridional wind component illustrate a downstream-propagating Rossby wave. To the east of *Tokage*, a pre-existing wave train can be seen from about 150°E at 0000 UTC on 17 October, weakening at about 60°W at 1200 UTC on 23 October. However, the wave emanating from the dipole around *Tokage*'s ET did not exist before. This suggests that it was excited by the ET. The dipole stretched downstream during the next three days, and from 1200 UTC on 23 October a downstream-propagating Rossby wave train has developed.

The regions of high uncertainty located at about 125°E from 1200 UTC on 17 October (Figure 7) are associated with the upstream trough and the ridge directly downstream of the ET system seen in the geopotential field at 200 hPa (Figure 4(e)). The signal broadens and travels to the east with the ridge. The weak signal in the upstream trough can be seen separately from 0000 UTC on 21 October until 0000 UTC on 23 October. From about 23 October the signal remains stationary around the cut-off low at about 180°E for two days and decreases in scale. At the end of the forecast interval, a positive signal has propagated with the Rossby

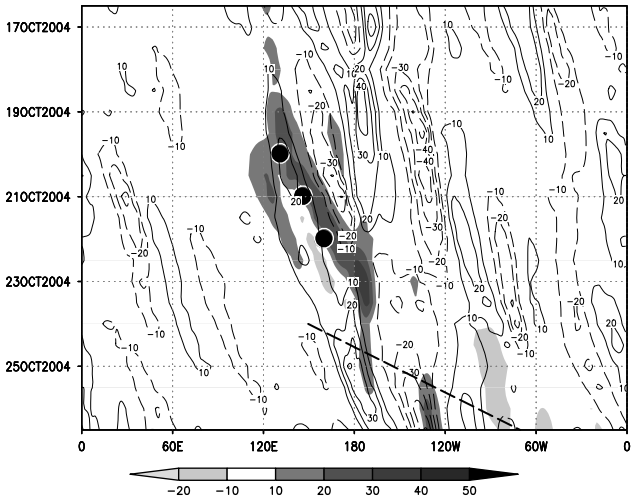

Figure 7. Hovmöller plot of the RMSD difference of the geopotential height at 200 hPa between the ensemble runs with and without targeted perturbations on *Tokage* (shaded, m). Shown are analysed meridional wind component (contours, m s^{-1}) averaged between 30°–60°N and the ten-day forecast from 1200 UTC on 16 October. The ET position and position of the ex-TC one day before ET and one day thereafter is marked by a black dot. The Rossby wave train excited by *Tokage* is marked by a black dashed line.

wave train and is located at 120°W. The highest increase of spread due to the targeted perturbations is associated with the ridge directly downstream of *Tokage* and is over 30% at 0000 UTC on 23 October.

The leading edge of the signal due to the targeted perturbations propagates with a speed of over 20° per day to the east (Figures 4 and 7), which is only about 66% of the signal propagation of 30° per day found by Szunyogh *et al.* (2002). This can be related to the work of Riemer *et al.* (2008), who found a reduced group velocity compared with previous studies when an ET was present in their idealized modelling study with a straight jet. They speculated that the ET system, which acts as a source of the wave train, moves more slowly than a developing baroclinic system would and hinders the upper-level wave propagation to the east.

4.1.2. Influence of ET dynamics

In this section we consider the processes leading to uncertainty in the formation of the trough–ridge–trough pattern found in the midlatitudes. Riemer *et al.* (2008) found that the ridge-building is partly due to the divergent flow at upper levels of a TC, but that the balanced flow associated with low upper-level potential vorticity (PV) plays a more important role in the formation of the ridge and especially the downstream trough. The question arises as to by what degree the TC outflow and the associated PV modification are connected to the latent heat release at the warm front of an ET and if, as a consequence, the low-level processes cause the low upper-level PV and the divergent flow.

During ET, warm moist tropical air is transported polewards at the east side of the decaying TC and rises over the tilted isentropes associated with the baroclinic zone in the midlatitudes. This process leads to enhanced ascent and precipitation in the warm front of the ET system. For example, Davis *et al.* (2008) found that the asymmetric vertical mass flux is larger during an ET. The enhanced precipitation in the warm front can diabatically modify the jet structure (Atallah and Bosart, 2003).

The growth of spread due to the low-level processes described above is investigated using the RMSD differences of temperature advection at 850 hPa and precipitation (Figure 8). The connection of the upper-level dynamics of ET to the growth of spread caused by these low-level processes is investigated with the aid of the horizontal wind at the dynamic tropopause.

One day prior to ET, a ridge in the dynamic tropopause north of *Tokage* can already be seen (Figure 8(a)). The rather symmetric pattern of strong precipitation at that time has mostly tropical character (Figure 8(b)). Although there is high variability in the precipitation, not much variability is seen at the dynamic tropopause at that time. A region of enhanced variability can be found only in the upstream region of the ridge. However, an RMSD signal was seen in the geopotential in the trough–ridge–trough pattern (Figure 4(c)). Hence, a small influence of the TC on the midlatitude flow can already be seen before ET, when the TC is still in its tropical stage. Small-scale positive signals in the temperature advection and in the precipitation are located close to the TC position until 1 day before ET (not shown).

At the ET time the area covered by the temperature signals has expanded rapidly in scale (Figure 8(c)). The positive small-scale structures in the temperature advection are associated with the wider variety of TC locations over southern Japan seen in the tracks of Pert/Nosto (Figure 2(a)). The position of the precipitation signal is consistent with that of the temperature advection but of coarser structure and stronger (Figure 8(d)). A few negative signals are seen as well, which are connected to the further northward accumulation of the TC positions seen in the tracks of Nopert/Nosto (Figure 2(b)). At that time a strong growth of signal in the geopotential was seen (Figure 4(e)).

Hence, as the quickly growing spread in the upper-level flow coincides with the strong growth of scale of the region influenced by low-level processes, we attribute the enhancement of the formation and uncertainty in the trough–ridge–trough pattern to the uncertainty in low-level temperature advection and precipitation.

We have illustrated the connection between the rapid growth of spread during ET due to the perturbations targeted for *Tokage* and the wider spread of TC positions in Pert/Nosto compared with Nopert/Nosto. In the following it will be shown that the larger range of TC intensities in Pert/Nosto causes more variability in the intensity of the diabatic processes and in the upper-level flow. For that purpose, the clusters obtained by applying the analysis method of Harr *et al.* (2008) on the potential temperature on the dynamic tropopause (Table I) of all the ensemble members are investigated.

The Pert/Nosto clusters vary more in terms of the central pressure of *Tokage*, the shape of the dynamic tropopause and the position of the TC relative to the potential temperature gradient at the dynamic tropopause than the clusters of Nopert/Nosto. In the Pert/Nosto experiment, one additional cluster was obtained compared with the other two experiments. Two of the clusters with the largest differences to each other for Pert/Nosto (Figure 9(a) and (b)) and Nopert/Nosto (Figure 9(c) and (d)) respectively are shown 12 h after ET, as the variability in the ensemble members has a maximum at that time (not shown). In the

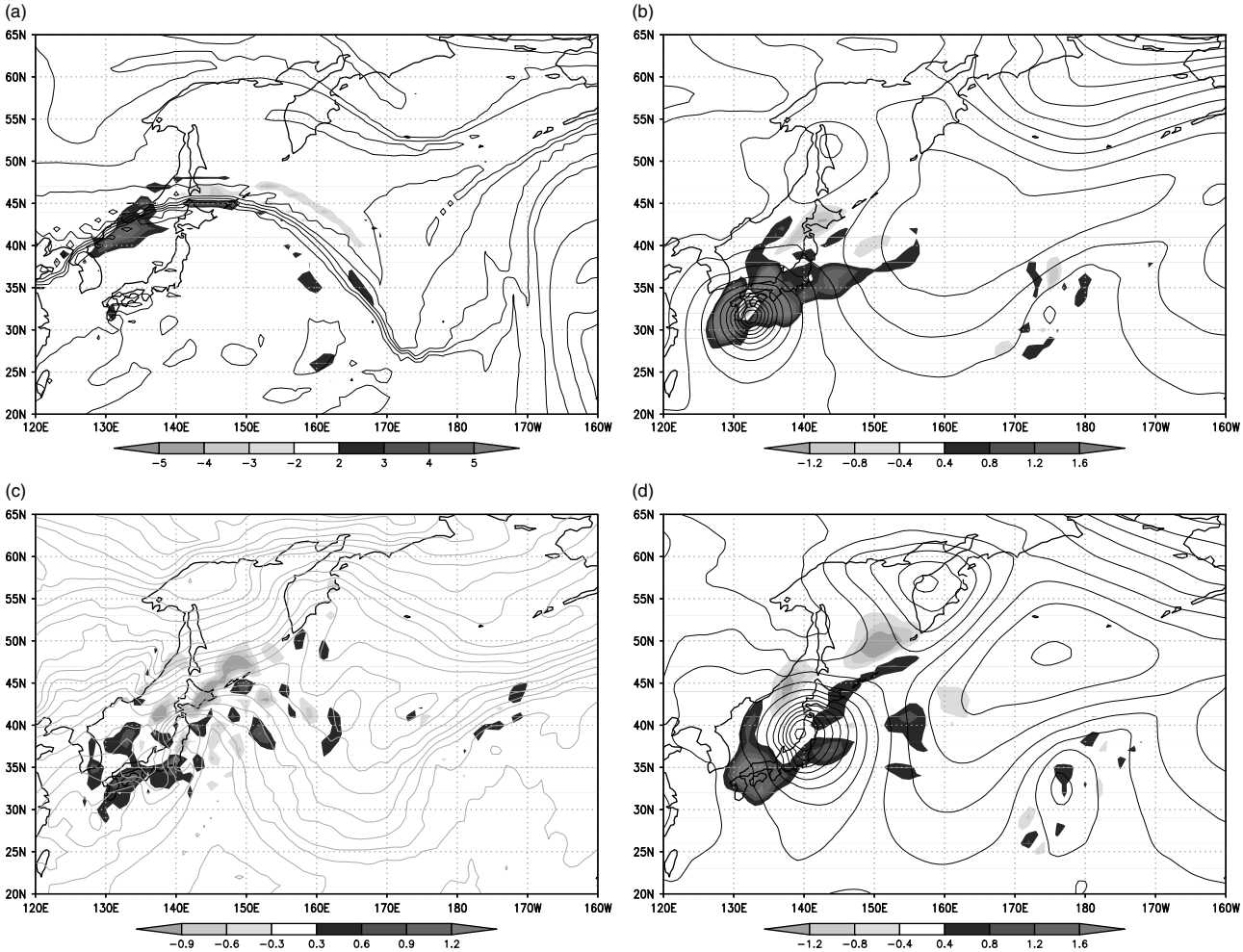

Figure 8. RMSD difference of (a) the horizontal wind at PVU = 2, (b) and (d) the surface precipitation ($m \times 10^2$) and (c) the temperature advection ($K \times 10^4$) at 850 hPa between the ensemble forecasts from 1200 UTC on 16 October with and without targeted perturbations on *Tokage* (shaded). Top: forecasts for 0000 UTC on 20 October, i.e. 24 h prior to ET. Bottom: forecasts for 0000 UTC on 21 October, i.e. ET time. ECMWF control forecasts of (a) the potential temperature on PVU = 2, (b) and (d) the mean-sea-level pressure (hPa, contours) and (c) the temperature at 850 hPa (K, contours).

following the cluster with the highest central pressure for a given experiment will be referred to as 'the weak cluster' and that with the deepest central pressure as 'the strong cluster'.

In the weak Pert/Nosto cluster with a central pressure of 1000 hPa (Figure 9(a)), the midlatitude potential temperature gradient on the dynamic tropopause is more zonal polewards of the ex-TC than in the cluster showing the deep central pressure of 970 hPa (Figure 9(b)). *Tokage* does not undergo reintensification in the former, while it reintensifies strongly in the latter cluster. The downstream trough is broader and has a weaker potential temperature gradient on the dynamic tropopause in the weak cluster of Pert/Nosto, while in the strong cluster of Pert/Nosto the distinct midlatitude ridge forms a cut-off low with strong potential temperature gradient.

Less differences in the central pressure of *Tokage* are seen in the Nopert/Nosto clusters. The amplitude of the ridge in the cluster showing the weaker system with a central pressure of 990 hPa (Figure 9(c)) is less than that of the cluster showing the deeper system with a central pressure of 975 hPa (Figure 9(d)). The potential temperature gradient on the dynamic tropopause in the downstream trough (Figure 9(c)) is weaker than that of the strong cluster of Nopert/Nosto (Figure 9(d)) as well. However, compared with Pert/Nosto, the weak cluster of Nopert/Nosto shows a stronger ET development and the strong cluster a weaker ET development.

The strength of temperature advection and consequently of the warm frontogenesis varies depending on the distance of the TC to the baroclinic zone in the individual ensemble members, and thus leads to different precipitation events in the members. We investigate the temperature advection and the precipitation in the individual clusters in an earlier stage of ET, i.e. 12 hours before the completion of ET at 1200 UTC on 20 October, and their impact on the upper-level flow during ET (Figure 10). Note that the diabatic processes are investigated 24 h earlier than the potential temperature at the dynamic tropopause.

In the cluster showing the decay of *Tokage* (the weak cluster of Pert/Nosto), small-scale positive values to the east and small-scale negative values to the west of the decaying *Tokage* are seen at about 130–140°E and 30–35°N, but no clear warm or cold front can be distinguished (Figure 10(a)). However, a band of precipitation is located north and northeast of the decaying system (Figure 11(a)) associated with the advection of tropical air. In the strong cluster of Pert/Nosto (Figure 10(b)) a strong warm front–cold front couplet is seen associated with the transitioning *Tokage*. The beginning of a cyclonic wrap-up of the low-level temperature field in the region of the cold front similar to that found

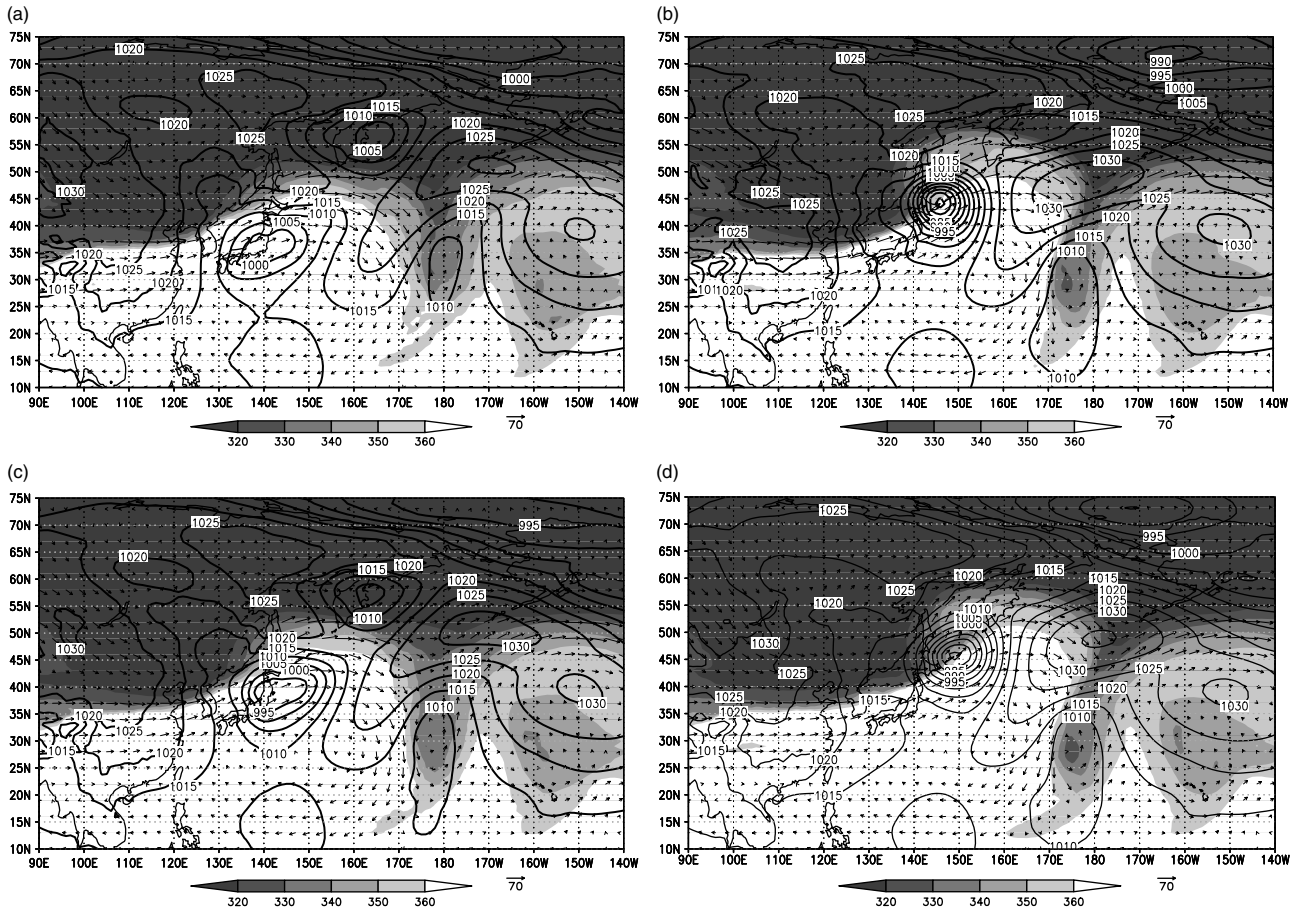

Figure 9. Two of four clusters for *Tokage* in Pert/Nosto (a, b) and two of three clusters in Nopert/Nosto (c, d) for the ensemble forecast from 1200 UTC on 16 October 2004 valid on 1200 UTC on 21 October, i.e. 12 h after ET. Cluster means of potential temperature on PVU = 2 (shaded) and cluster means of mean-sea-level pressure (hPa, contours) are shown.

by Shapiro and Keyser (1990) can be seen. Consistent with the strong warm front, a region of strong precipitation is located northeast of the ET system, slightly ahead of the warm advection (Figure 11(b)).

The weak cluster of Nopert/Nosto shows a weak warm front and a slightly stronger cold front between 130–150°E and 30–40°N (Figure 10(c)) associated with the temperature advection due to ex-*Tokage*. The temperature advection in the strong cluster of Nopert/Nosto (Figure 10(d)) is almost of the same intensity as in the strong cluster of Pert/Nosto (Figure 10(b)). The beginning of a cyclonic wrap up is seen in the strong cluster of Nopert/Nosto as well. For the weak cluster of Nopert/Nosto (Figure 11(c)) a band of precipitation similar to the weak cluster of Pert/Nosto (Figure 11(a)) can be found. However, the amount is higher in the Nopert/Nosto cluster as the warm, moist air advected to the east of the ET system ascends over more strongly tilted isentropic surfaces due to the stronger baroclinic zone. This leads to enhanced convection to the eastern side of the system. The precipitation amount and scale in the strong cluster of Nopert/Nosto (Figure 11(d)) is similar to that in the strong cluster of Pert/Nosto (Figure 11(b)).

The evolution of the intensities of the ETs and the associated tropopause shapes for all the Pert/Nosto and Nopert/Nosto clusters can be compared using spaghetti plots of the cluster means. On 1200 UTC on 20 October, i.e. 12 h prior to ET, the slightly different amplitudes of the ridges correlate well with the proximity of the TC central pressures to the upstream midlatitude troughs. The closer the central pressures are relative to the tropopause gradients, the higher the ridges and the downstream troughs are, both for Pert/Nosto and for Nopert/Nosto (Figure 12(a) and (b)). At that time the variability in Pert/Nosto (Figure 12(a)) is only slightly stronger than that of Nopert/Nosto (Figure 12(b)). This is consistent with the only slightly higher spread in the wind on the dynamic tropopause (Figure 8(a)) and the relatively weak signal in the geopotential at 0000 UTC on 20 October (Figure 4(c)).

At ET time, high variability in the location of the central pressure of *Tokage* and in the shift and amplitude of the upper-level ridge and the downstream trough can be seen both for Pert/Nosto (Figure 12(c)) and Nopert/Nosto (Figure 12(d)). The variability in Pert/Nosto, however, is higher due to the additional cluster showing the decay (solid). The low amplitude of the ridge in this weak Pert/Nosto cluster is obviously connected to the weak interaction with the baroclinic zone and the associated weak latent heat release through precipitation (Figure 11(a)). The strong latent heat release through the high precipitation amounts in the Pert/Nosto cluster showing the strong ET (Figure 11(b)) modifies the ridge diabatically and leads to a high-amplitude ridge–trough pattern (Figure 12(c), dot–dashed). The high variability in Pert/Nosto is clearly associated with the wide distribution of the TC centres at the ET time (Figure 3(a)). The members showing *Tokage* located over South Japan, which are not seen in the other two experiments, are responsible for the weak cluster (Figure 3(b) and (c)).

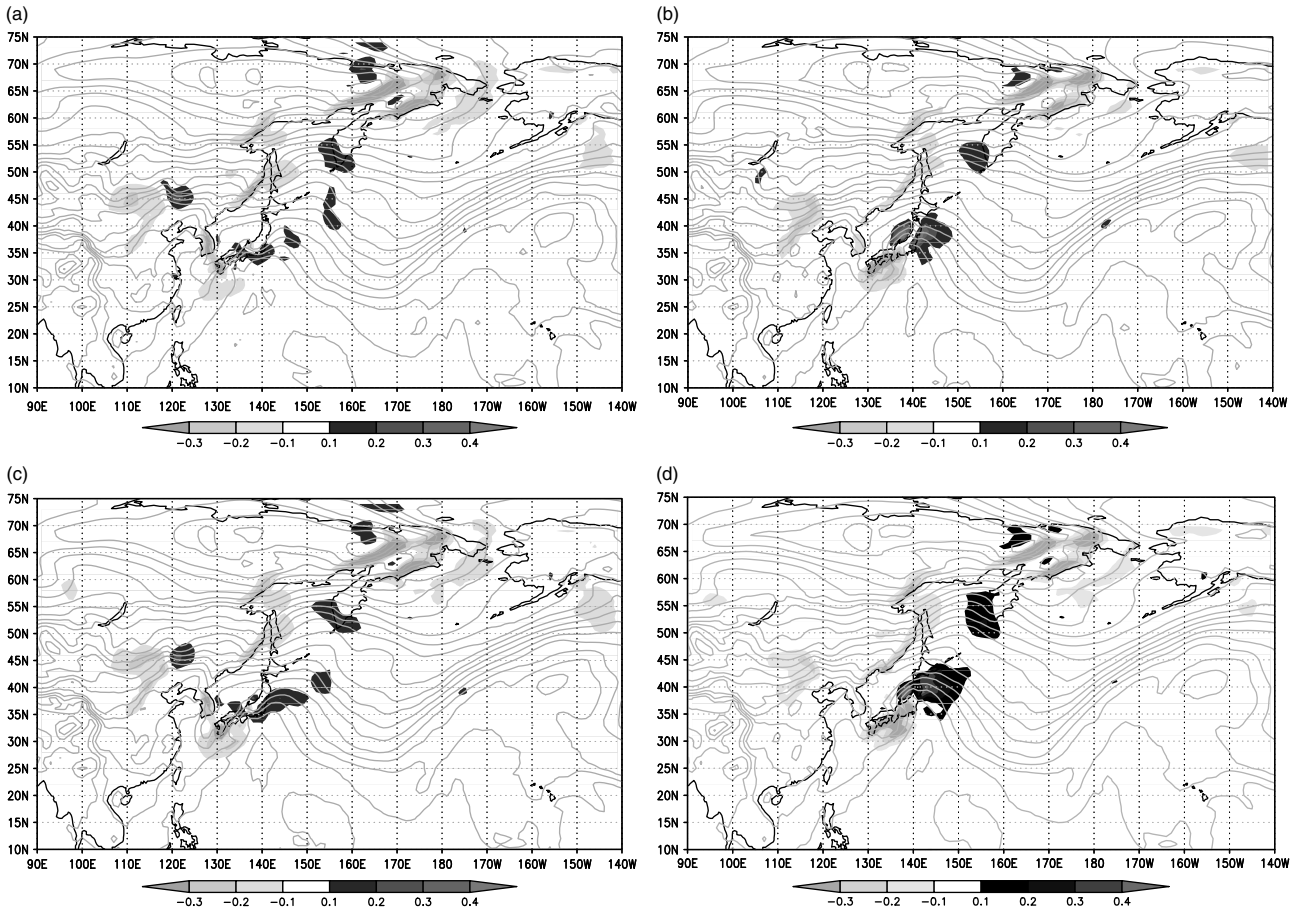

Figure 10. Same clusters as Figure 9 but for 1200 UTC on 20 October. Cluster means of temperature advection at 850 hPa (K, shaded) and cluster means of temperature at 850 hPa (K $\times$ 10^4, contours) are shown.

Through the clustering we see that strong ET systems located close to the upstream trough lead to high-amplitude ridging and troughing downstream. The case of the weak tropical cyclone separated from the upstream trough is associated with a more zonal midlatitude pattern. Thus, the presence of the weak cluster in Pert/Nosto leads to higher variability in the midlatitude flow. In an inspection of the temporal evolution of the potential temperature on the dynamic tropopause (not shown), it was striking that one maximum of tropopause potential temperature, which was located directly above the region of strong precipitation, was transported into the downstream trough in all the clusters. This maximum enhanced the gradient of the potential temperature in the downstream trough in the two strongest clusters (Figure 12(c) and (d), dot–dashed and dotted lines). This is one mechanism by which the influence of the ET travelled downstream.

The variability is partly due to differences in the timing, i.e. some clusters show quicker transformations and reintensification than others. However, the developments in the individual clusters seen 36 h after ET (Figure 12(e) and (f), solid and dashed lines) give evidence that the amplitude of the ridge is in fact smaller and no cut-off lows form from the downstream trough in the weak clusters.

We conclude that the targeted perturbations yield a larger number of possible ET scenarios to account for the uncertainty associated with the ET of *Tokage*. The ensemble forecast without the targeted perturbations would assign too high a probability to an incorrect forecast. The targeted perturbations lead to a phase shift, i.e. a reduced phase speed, of the trough–ridge–trough pattern in the ensemble members compared with the members in the runs without targeted perturbations.

A strong relation was seen between the strength of diabatic processes in the ET system and the steepness of the upper-level ridge north of *Tokage* in the midlatitude flow. Furthermore, the development of the downstream trough depended on the strength of the diabatic processes and the ridge.

Hence, evidence was given that the upper-level flow is modified by the ET of *Tokage* and that the uncertainty in the midlatitude flow introduced by the ET propagates downstream. The strength of latent heat release is closely connected to the horizontal wind associated with the low upper-level PV, which in turn modifies the downstream trough. Consequently, the latent heat release influences the development of the downstream trough.

The growth of the targeted perturbations due to the tropical SVs that are optimized within the 48 h interval from 1200 UTC on 16 October to 1200 UTC on 18 October is strongly enhanced during the ET time. Thus, the ET plays an important role in generating uncertainty and propagating it downstream.

4.2. Signal of the stochastic physics

4.2.1. Origin and downstream propagation

Until one day before ET time (Figure 13(a)), small localized influences of the stochastic physics can be seen distributed

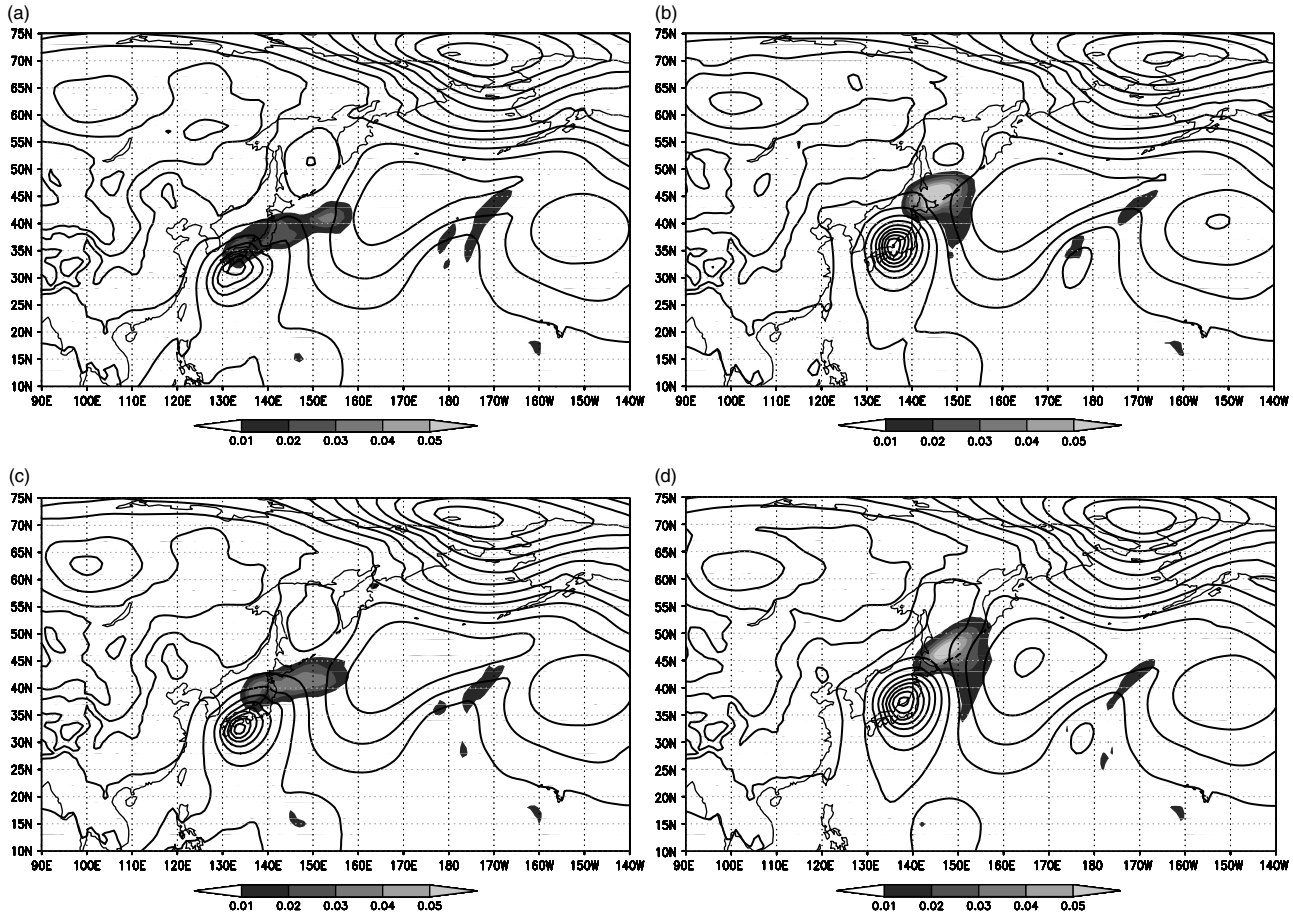

Figure 11. Same clusters and time as Figure 10 but for cluster means of surface precipitation ($m \times 10^2$, shaded) and mean-sea-level pressure (hPa, contours).

over the whole western North Pacific and partly over North America at 200 hPa. At this level and forecast time, parametrized processes associated with the TC seem to be no more important than those in the midlatitude flow that are not localized close to the ET system. Hence, the generation of the spread in the 200 hPa geopotential height in the vicinity of the ET event is almost entirely associated with the targeted perturbations. At 500 hPa (Figure 13(b)), a clear signal can be seen at the location of *Tokage*. On the one hand, this is due to the slightly wider distribution of TC positions in the ensemble than in Nopert/Nosto (Figure 2(b) and (c)). On the other hand, the strong convection within a TC is almost entirely parametrized in global forecast models because of its small scales. Consequently, the higher spread in the vicinity of *Tokage* may be generated through the perturbation of temperature and humidity tendencies by the stochastic physics. The influence of the targeted perturbations, however, is larger than that of the stochastic physics one day before ET (Figures 4(d) and 13(b)).

At ET time, three regions of high-amplitude signal in the stochastic physics can be seen at 200 hPa (Figure 13(c)). These have grown strongly in the previous 24 h and are fairly confined. One part is associated with variability in the midlatitude trough upstream of *Tokage*. The largest part of the signal in scale and amplitude at ET time is seen downstream of *Tokage*. It is associated with higher variability in the representation of the ridge. The signal up- and downstream of *Tokage* is still smaller in scale and amplitude than the signal due to the targeted perturbations at ET time (Figure 4(e)). As seen in the track forecasts, the positions of the TCs and their intensity vary more in the ensemble runs with targeted perturbations (Figures 2(a) and 3(a)) than in those with stochastic physics (Figures 2(c) and 3(c)) at the ET time, causing the higher variations visible in the geopotential fields. The third part of the signal in Nopert/Sto is further downstream at about 150°W and 55°N and almost stationary. It has grown strongly from 0000 UTC on 20 October and is not connected with the ET event.

The most extreme members selected form the Nopert/Sto clusters (Table I) show that the regions of largest spread in Nopert/Sto (black) are shifted only slightly compared with those in Nopert/Nosto (grey) (Figure 14). There are weak negative parts of the signal in the regions of the TC, but not of the magnitude seen between Pert/Nosto and Nopert/Nosto (Figure 4).

The signal in the stochastic physics is associated with the Rossby wave train influenced by *Tokage*'s ET (Figure 15) but it starts to grow later and more slowly compared with that due to the targeted perturbations (Figure 7). The maximum values are smaller than those due to the targeted perturbations at 200 hPa (Figures 15 and 7(a)), but the signal continues growing when that due to the targeted perturbations is already reduced. The signals associated with *Tokage*'s ET propagate downstream as well. Three signals due to the stochastic physics have grown distinctly at about 0000 UTC on 25 October

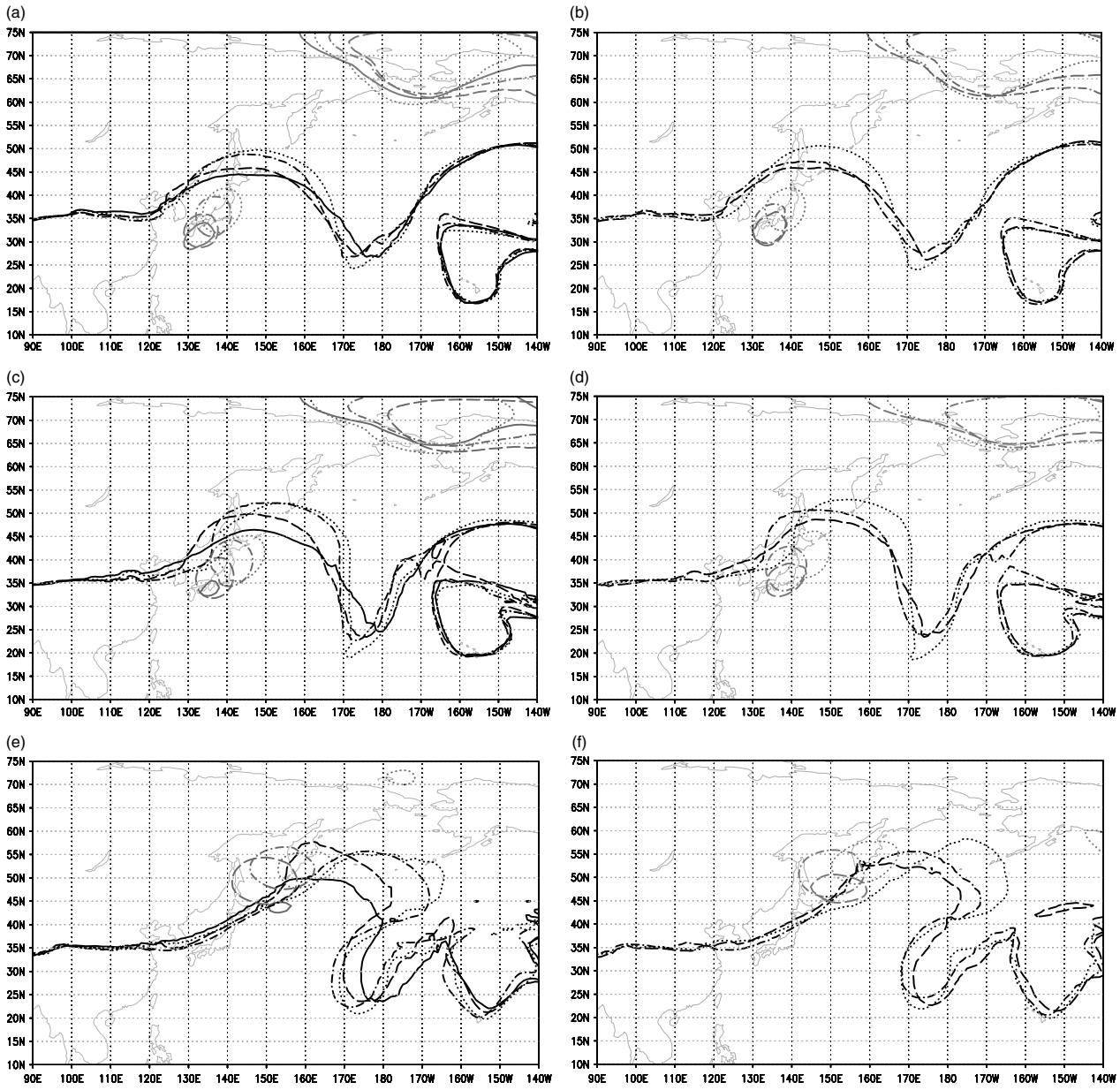

Figure 12. Spaghetti plots of the 350 K isentrope at PVU = 2 (black) and the 995 hPa surface pressure isobar (grey) of the cluster means for the forecasts from 1200 UTC on 16 October, verified at (top) 1200 UTC on 20 October, (middle) 0000 UTC on 21 October and (bottom) 1200 UTC on 22 October, for (left) Pert/Nosto (solid line is the weak cluster, dot–dashed line is the strong cluster) and (right) Nopert/Nosto (dashed line is the weak cluster, dot–dashed line is the strong cluster).

(Figure 15), i.e. at a time when the signal due to the targeted perturbations is reduced in scale (Figure 7). The increase of spread due to the stochastic physics attains maximum values of about 20% at 0000 UTC on 25 October.

4.2.2. Influence of ET dynamics

The RMSD differences of the surface precipitation between the experiments with and without stochastic physics one day prior to and at ET (not shown) exhibit signals of smaller intensity and much smaller scale than those seen between Pert/Nosto and Nopert/Nosto. Again, this can be attributed to the smaller spread in TC positions at the ET time. Nevertheless, a growth in scale of the signal from one day prior to ET to ET occurs. The signal in the temperature advection at 850 hPa due to the stochastic physics (not shown) is similar, but covers a slightly smaller region compared with that due to the targeted perturbations.

As for the targeted perturbations, we can attribute the enhanced spread due to the stochastic physics in the upper-level flow to the enhancement of spread in precipitation during ET. Further, it becomes clear that the stochastic physics is of less importance in generating spread in precipitation during ET than the diabatic targeted SVs. This result is not self-evident, as the stochastic physics is designed to perturb small-scale parametrized processes, which play an important role during ET.

After inspection of the clusters for Nopert/Sto (not shown) we see that the lower variability in track and intensity for Nopert/Sto leads to less variability in the low-level temperature advection and precipitation. In particular, comparison of the weak clusters for Pert/Nosto and Nopert/Sto shows that the weak cluster of Nopert/Sto

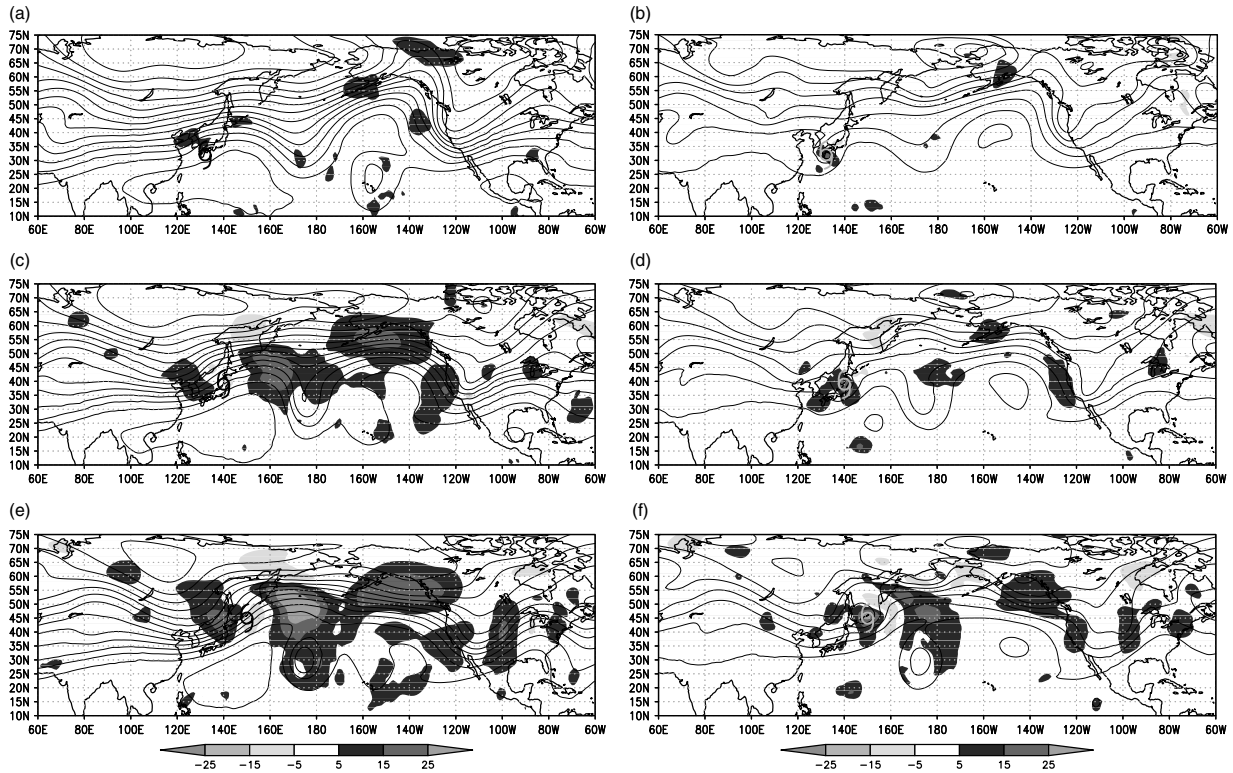

Figure 13. Same as Figure 4, but for ensemble runs with and without stochastic physics. Forecasts for (a,b) 0000 UTC on 20 October, i.e. 24 h prior to ET, (c,d) 0000 UTC on 21 October, i.e. ET time and (e,f) 0000 UTC on 22 October, i.e. 24 h after ET.

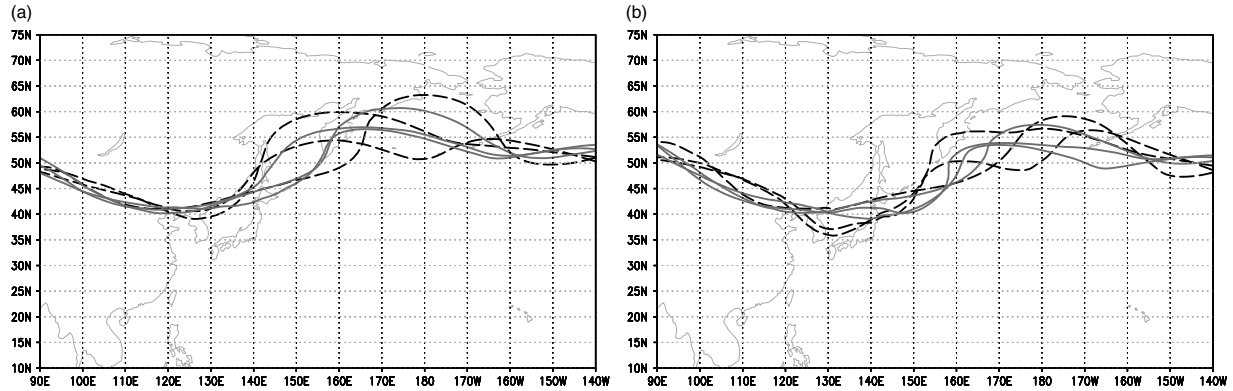

Figure 14. As Figure 5 but for Nopert/Sto (black, dashed) and Nopert/Nosto (grey) ensemble members initialized at 1200 UTC on 16 October, verified at 0000 UTC on 22 October, i.e. 24 h after ET, at (a) 200 hPa and (b) 500 hPa.

exhibits a stronger ET, higher amplitude ridging, a slightly stronger couplet of positive and negative temperature advection at 850 hPa and stronger precipitation over a broader area. These features are rather similar in the strong clusters of each experiment, emphasizing the lower variability in Nopert/Sto.

Spaghetti plots of the evolution of the Nopert/Sto clusters show that the variability in Nopert/Sto seen in the central pressures and in the ridges is similar to that in Nopert/Nosto. The variability is small 12 h before ET, but a higher variability in the ridges and the TC pressure centres is seen at the ET time. As in Pert/Nosto and Nopert/Nosto, when the TC is closer to the upstream trough the ridge is steeper at the ET time. The spread in the downstream trough is much smaller than in Pert/Nosto. It is of about the same size as in Nopert/Nosto, which is confirmed by the RMSD of the geopotential, in which no signal is seen in the downstream trough at about 170°–180°E and 20–35°N at the ET time (Figure 13(c)). Hence, there is almost no propagation of uncertainty from the ridge associated with *Tokage* into the downstream trough.

We can summarize that the smaller spread in the ensemble forecast with only the stochastic physics perturbations around *Tokage* leads to a smaller number of ET scenarios than in the ensemble forecast with the targeted perturbations. A particularly weak cluster is not identified. The reintensification after ET is deeper in the ensemble members due to the perturbations with stochastic physics.

The generation of spread due to the stochastic physics is caused both by the wider distribution of TC positions and by the higher intensity variations and higher variations in the diabatic processes compared with Nopert/Nosto.

As for Pert/Nosto and Nopert/Nosto, the amplitude of the ridge is tied to the strength and relative position of the TC. The impact of latent heat release on the modification of the upper-level ridge is confirmed. A downstream propagation

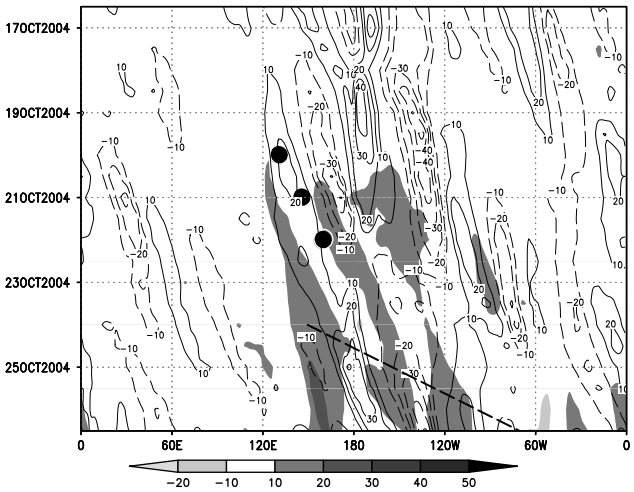

Figure 15. As Figure 7 but for the RMSD difference between the ensemble runs with and without stochastic physics without targeted perturbations on *Tokage* (shaded, m).

of the uncertainties in the ridge is not evident. No phase shift in the ensemble forecast with stochastic physics is seen compared with the runs with neither targeted perturbations nor stochastic physics.

4.3. Signal of both perturbation methods

4.3.1. Origin and downstream propagation

The signal of the targeted perturbations under the influence of stochastic physics, i.e. between Pert/Sto and Nopert/Sto (not shown), is very similar to that without the influence of stochastic physics, i.e. between Pert/Nosto and Nopert/Nosto (Figure 4). However, from one day before ET time the amplitude of the signal is slightly smaller. The values of changed spread occur at about the same position as in Figure 4, but the magnitudes are slightly lower.

The signal of the stochastic physics under the influence of targeted perturbations, i.e. between Pert/Sto and Pert/Nosto, is very similar to that between Nopert/Sto and Nopert/Nosto (Figure 13), but the amplitude is slightly smaller also. Hence, the two perturbation methods do not seem to interact with each other.

4.3.2. Influence of ET dynamics

In Pert/Sto four clusters are found (Table I), as in Pert/Nosto. However, the cluster containing the system with the weakest central pressure in Pert/Sto shows values below 995 hPa. The reintensification is moderate (Table I).

As indicated by the slightly smaller spread in Pert/Sto than in Pert/Nosto, the weakest cluster of Pert/Sto (not shown) shows less difference in central pressure from the other clusters. The shape of the tropopause in that cluster is similar to the weak cluster in Pert/Nosto. However, the base of the trough upstream of *Tokage* is slightly further south and the western part of the ridge directly downstream is slightly steeper. The TC in Pert/Sto is located slightly further to the southwest and it moves more slowly than in Pert/Sto. Apparently, the position of *Tokage* relative to the upstream trough is more favourable for intensification. Hence, *Tokage* weakens less during ET and reintensifies moderately thereafter.

5. Conclusions

In this study, EPS experiments for the specific ET case of *Tokage* (2004) were carried out because this typhoon seemed to have a very active influence on the formation of a characteristic trough–ridge–trough pattern inherent in some ET events (Anwender *et al.*, 2008). The aim was to compare separately the influence of targeted perturbations and stochastic physics on the dynamic representation of the ET event in the individual ensemble members. These two perturbation methods should further yield a means to quantify the dispersion of the effects due to an ET.

The EPS experiments showed that sufficient ensemble spread in the track and improved spread in the intensity forecast depends strongly on the additional perturbations targeted on *Tokage*. Without these, the track spread in the forecasts, especially that around the recurvature and ET of *Tokage*, was underestimated and the analysis was not encompassed by the ensemble members. The targeted perturbations were responsible for a wider spread including more ET scenarios. This is in contrast to earlier studies, which focused on the track and intensity prediction of the tropical cyclone (Puri *et al.*, 2001). The stochastic physics also led to a slightly higher spread, and to more deepening of the ex-TC in most of the ensemble members compared with the runs with neither targeted perturbations nor stochastic physics.

The impact of the SVs targeted on *Tokage* propagates downstream with a Rossby wave train that has been excited by the interaction of *Tokage* with the midlatitudes. The amplitude of the wave packet determines the transport of wave energy, which can trigger cyclogenesis far away from the ET event. At 20° per day the uncertainty associated with the ET propagates slightly more slowly than found by Szunyogh *et al.* (2002). An upstream phase shift in the ensemble members and consequently a reduction in phase speed due to the targeted perturbations was also visible. This confirms the findings of Riemer *et al.* (2008) that an ET event can slow down the propagation of a Rossby wave train.

The strong growth of the impact due to the targeted perturbations is associated with the rapid increase of uncertainty in TC tracks during ET. The resulting wider variety of TC locations relative to the baroclinic zone leads to stronger differences in latent heat release, which in turn yield a larger variety of representations of the trough–ridge–trough pattern in the upper-level flow.

This is confirmed using the analysis method of Harr *et al.* (2008) to group the ensemble members into clusters. In these clusters the temperature advection and precipitation amounts were closely connected with the amplitude of the trough–ridge–trough pattern in the midlatitudes north of *Tokage*. Thereby we can deduce that the low-level processes during *Tokage*'s ET modify the upper-level flow. The higher uncertainty due to the targeted perturbations is expressed through an additional cluster in the Pert/Nosto experiment, which shows a decay of *Tokage* without ET. This is the only cluster that shows a weaker development than the analysis. Hence, the analysis is included in the ensemble only through the targeted perturbations. Note, however, that in the clusters of the experiment with both perturbation methods the additional cluster also shows a system stronger than in the analysis. In the case of *Tokage*, the analysis

might have been inaccurate, as seen when comparing the ET positions of analysis and best track.

The distinct growth of the effect due to the stochastic physics in the vicinity of the ET and in the downstream ridge is also associated with the increase of uncertainty in the TC locations. The uncertainty introduced by the stochastic physics is smaller, and no reduction in phase speed is seen compared with the runs without stochastic physics.

As in the runs perturbed by the targeted SVs, the correlation between the latent heat release at low levels and the amplitude of the upper-level flow is manifest. The growth of the ensemble spread due to stochastic physics is slower but it continues beyond the medium range.

Apparently, the EPS had serious problems in predicting the weakening of Typhoon *Tokage* after landfall. The weakening found through the additional targeted perturbations seems to play an essential role in improving the forecast. Other case studies of the representation of an ET's intensity in the EPS during landfall on mountainous islands would be interesting, to assess the quality of ensemble prediction in such a case and the associated impact on the predictability.

We have demonstrated that experiments with an operational EPS can yield insightful information about the sensitivity of numerical forecasts to an ET event and the impact that such events can have on the predictability far downstream. Further experiments examining different ET cases are needed to test the robustness of these results, given the large variety in ET development. It would also be of interest to test the stochastic kinetic energy backscatter scheme (Berner *et al.*, 2009) that is being developed at ECMWF. This scheme represents model uncertainty associated with near-grid-scale variability that is not adequately represented but has an effect on the resolved scales. A future study will consider the influence of higher resolution on both SVs and EPS forecasts.

Acknowledgements

This study was sponsored by the Office of Naval Research, Marine Meteorology Program. Acknowledgment is made for the use of ECMWF's computing and archive facilities through the special project 'The impact of tropical cyclones on extratropical predictability'. We are grateful to Carsten Maass and his colleagues at ECMWF user support for their help in setting up the experiments with the ECMWF model. We gratefully acknowledge two anonymous reviewers for thoughtful and thorough reviews.

References

Anwender D, Harr PA, Jones SC. 2008. Predictability associated with the downstream impacts of the extratropical transition of tropical cyclones: Case studies. *Mon. Weather Rev.* **136**: 3226–3247.

Atallah EH, Bosart LF. 2003. The extratropical transition and precipitation distribution of Hurricane Floyd (1999). *Mon. Weather Rev.* **131**: 1063–1081.

Barkmeijer J, Buizza R, Palmer TN, Mahfouf JF. 2001. Tropical singular vectors computed with linearized diabatic physics. *Q. J. R. Meteorol. Soc.* **127**: 685–708.

Berner J, Shutts GJ, Leutbecher M, Palmer TN. 2009. A spectral stochastic kinetic energy backscatter scheme and its impact on flow-dependent predictability in the ECMWF ensemble prediction system. *J. Atmos. Sci.* **66**: 603–626.

Buizza R, Miller M, Palmer TN. 1999. Stochastic representation of model uncertainties in the ECMWF ensemble prediction system. *Q. J. R. Meteorol. Soc.* **125**: 2887–2908.

Davis CA, Jones SC, Riemer M. 2008. Hurricane vortex dynamics during Atlantic extratropical transition. *J. Atmos. Sci.* **65**: 714–736.

Farrell BF. 1982. The initial growth of disturbances in a baroclinic flow. *J. Atmos. Sci.* **39**: 1663–1686.

Harr PA, Anwender D, Jones SC. 2008. Predictability associated with the downstream impacts of the extratropical transition of tropical cyclones: Methodology and a case study of Typhoon Nabi (2005). *Mon. Weather Rev.* **136**: 3205–3225.

corpauJMA. 2004.. Japan Meteorological Agency. http://www.jma.go.jp/jma/indexe.html.

Jones SC, Harr PA, Abraham J, Bosart LF, Bowyer PJ, Evans JL, Hanley DE, Hanstrum BN, Hart RE, Lalaurette F, Sinclair MR, Smith RK, Thorncroft C. 2003. The extratropical transition of tropical cyclones: Forecast challenges, current understanding, and future directions. *Weather and Forecasting* **18**: 16–56.

Klein PM, Harr PA, Elsberry RL. 2000. Extratropical transition of western North Pacific tropical cyclones: An overview and conceptual model of the transformation stage. *Weather and Forecasting* **15**: 373–395.

Klein PM, Harr PA, Elsberry RL. 2002. Extratropical transition of western North Pacific tropical cyclones: Midlatitude and tropical cyclone contributions to re-intensification. *Mon. Weather Rev.* **132**: 2240–2259.

Leutbecher M. 2007. On the representation of initial uncertainties with multiple sets of singular vectors optimized for different criteria. *Q. J. R. Meteorol. Soc.* **133**: 2045–2056.

Leutbecher M, Palmer TN. 2008. Ensemble forecasting. *J. Comp. Phys.* **227**: 3515–3539.

Lewis JM. 2005. Roots of ensemble forecasting. *Mon. Weather Rev.* **133**: 1865–1885.

McTaggart-Cowan R, Gyakum JR, Yau MK. 2003. The influence of the downstream state on extratropical transition: Hurricane Earl (1998) case study. *Mon. Weather Rev.* **131**: 1910–1929.

McTaggart-Cowan R, Gyakum JR, Yau MK. 2004. The impact of tropical remnants on extratropical cyclogenesis: Case study of Hurricanes Danielle and Earl (1998). *Mon. Weather Rev.* **132**: 1617–1636.

Puri K, Barkmeijer J, Palmer TN. 2001. Ensemble prediction of tropical cyclones using targeted diabatic singular vectors. *Q. J. R. Meteorol. Soc.* **127**: 709–731.

Riemer M, Jones SC, Davis CA. 2008. The impact of extratropical transition on the downstream flow: an idealised modelling study with a straight jet. *Q. J. R. Meteorol. Soc.* **134**: 69–91.

Ritchie EA, Elsberry RL. 2007. Simulations of the extratropical transition of tropical cyclones: Phasing between the upper-level trough and tropical cyclones. *Mon. Weather Rev.* **135**: 862–876.

Shapiro M, Keyser D. 1990. 'Fronts, jet streams and the tropopause'. In *Extratropical Cyclones. The Erik Palmén Memorial Volume*, Newton CW, Holopainen EO (eds). Amer. Meteorol. Soc.: Boston, MA; pp 167–191.

Szunyogh I, Toth Z, Zimin AV, Majumdar SJ, Persson A. 2002. Propagation of the effect of targeted observations: The 2000 winter storm reconnaissance program. *Mon. Weather Rev.* **130**: 1144–1165.

